



# Continuously increasing $\delta^{98}\text{Mo}$ values in Neoarchean black shales and iron formations from the Hamersley Basin

Florian Kurzweil<sup>a,\*</sup>, Martin Wille<sup>a</sup>, Ronny Schoenberg<sup>a</sup>, Heinrich Taubald<sup>a</sup>,  
Martin J. Van Kranendonk<sup>b</sup>

<sup>a</sup> Eberhard Karls University of Tuebingen, Department of Geosciences, Wilhelmstraße 56, 72074 Tuebingen, Germany

<sup>b</sup> School of Biological, Earth and Environmental Sciences and Australian Centre for Astrobiology, University of New South Wales, Kensington, NSW 2052, Australia

Received 2 September 2014; accepted in revised form 4 May 2015; available online 14 May 2015

## Abstract

We present Mo-, C- and O-isotope data from black shales, carbonate- and oxide facies iron formations from the Hamersley Group, Western Australia, that range in age from 2.6 to 2.5 billion years. The data show a continuous increase from near crustal  $\delta^{98}\text{Mo}$  values of around 0.50‰ for the oldest Marra Mamba and Wittenoom formations towards higher values of up to 1.51‰ for the youngest sample of the Brockman Iron Formation. Thereby, the trend in increasing  $\delta^{98}\text{Mo}$  values is portrayed by both carbonate facies iron formations and black shales. Considering the positive correlation between Mo concentration and total organic carbon, we argue that this uniformity is best explained by molybdate adsorption onto organic matter in carbonate iron formations and scavenging of thiomolybdate onto sulfurized organic matter in black shales. A temporal increase in the seawater  $\delta^{98}\text{Mo}$  over the period 2.6–2.5 Ga is observed assuming an overall low Mo isotope fractionation during both Mo removal processes. Oxide facies iron formations show lowest Mo concentrations, lowest total organic carbon and slightly lower  $\delta^{98}\text{Mo}$  compared to nearly contemporaneous black shales. This may indicate that in iron formation settings with very low organic matter burial rates, the preferential adsorption of light Mo isotopes onto Fe-(oxyhydr)oxides becomes more relevant.

A similar Mo-isotope pattern was previously found in contemporaneous black shales and carbonates of the Griqualand West Basin, South Africa. The consistent and concomitant increase in  $\delta^{98}\text{Mo}$  after 2.54 billion years ago suggests a more homogenous distribution of seawater molybdate with uniform isotopic composition in various depositional settings within the Hamersley Basin and the Griqualand West Basin. The modeling of the oceanic Mo inventory in relation to the Mo in- and outflux suggests that the long-term build-up of an isotopically heavy seawater Mo reservoir requires a sedimentary sink for isotopically light Mo. The search for this sink (i.e. adsorption onto Mn-oxides in well oxygenated surface oceans and/or subaerial environments or incomplete thiomolybdate formation in weakly sulfidic settings) remains debated, but its relevance becomes more important closer to the Great Oxidation Event and is probably related to already weakly oxidizing conditions even prior to the 2.5 Ga “whiff of oxygen”.

© 2015 Elsevier Ltd. All rights reserved.

## 1. INTRODUCTION

The exact timing and evolution of the oxygenation of Earth's atmosphere and oceans still remain debated in the scientific community. The generally accepted model is of a

\* Corresponding author. Tel.: +49 70712972601; fax: +49 7071295713.

E-mail address: [florenzweil@hotmail.de](mailto:florenzweil@hotmail.de) (F. Kurzweil).

Great Oxidation Event (GOE) between 2.45 and 2.32 Ga (Bekker et al., 2004; Hannah et al., 2004; Holland, 2006) when atmospheric oxygen levels rose above  $10^{-5}$  of present atmospheric level (PAL) (Farquhar et al., 2000; Pavlov and Kasting, 2002). This view has been challenged by more recent studies that suggest at least locally a much earlier first appearance of free atmospheric oxygen, which was most likely subjected to strong fluctuations (Anbar et al., 2007; Wille et al., 2007; Frei et al., 2009; Duan et al., 2010; Voegelin et al., 2010; Crowe et al., 2013; Kurzweil et al., 2013; Reinhard et al., 2013; Planavsky et al., 2014). These (temporal) increases in atmospheric oxygen levels were tightly coupled with surface ocean oxygenation and the development of a stratified water column with anoxic deep waters (Reinhard et al., 2009; Kendall et al., 2010). However, the possible causes for environmental oxygenation during Meso- to Neoproterozoic are still a matter of debate, as described in detail by Catling (2014).

Due to their redox sensitive behavior, some transition metals (V, Cr, Fe, Mo, Re) and, particularly, their isotopic variations, can be used as proxies for environmental redox changes. Molybdenum, dissolved as molybdate ( $\text{MoO}_4^{2-}$ ), is one of the most abundant transition metals in the modern oxygenated oceans. Its long residence time between 440 and 750 kyrs, depending on fluxes and mass balance calculations (Morford and Emerson, 1999; Miller et al., 2011), results in a globally homogeneous modern seawater Mo-isotopic composition of  $2.3\text{‰}$  in  $\delta^{98}\text{Mo}$  (Siebert et al., 2003). This seawater  $\delta^{98}\text{Mo}$  value is in stark contrast with an average  $\delta^{98}\text{Mo}$  value of  $0.4\text{‰}$  of the upper continental crust (Voegelin et al., 2014), the main source of oceanic Mo. The build-up of an isotopically heavy Mo oceanic reservoir is associated with Mo isotopic fractionation during adsorption of  $\text{MoO}_4^{2-}$  onto mineral surfaces. Recent X-ray absorption spectroscopy studies (XANES and EXAFS) show that the coordination of tetrahedrally coordinated molybdate ( $\text{MoO}_4^{2-}$ ) may change during adsorption (Wasylenko et al., 2008; Kashiwabara et al., 2011). With this, adsorbed Mo forms outer sphere complexes on ferrihydrite and Al-oxides that are partly tetrahedrally and partly octahedrally coordinated. By contrast, Mo forms inner sphere complexes on Mn- and Ti-oxides that are octahedrally coordinated (Kashiwabara et al., 2011). The Mo-coordination is of particular interest for Mo-isotope studies, as octahedrally bound Mo has longer and therefore weaker Mo–O bonds than tetrahedrally bound Mo. As a consequence, isotopically light Mo is preferentially incorporated into octahedral coordination sites. Therefore, adsorption onto Mn-oxides causes large differences in the Mo-isotopic composition ( $\Delta^{98}\text{Mo}_{\text{Mn-oxides-seawater}} = \delta^{98}\text{Mo}_{\text{Mn-oxides}} - \delta^{98}\text{Mo}_{\text{seawater}} = -3\text{‰}$ ; Barling et al., 2001), whereas the difference is somewhat smaller when molybdate adsorbs onto ferrihydrite ( $\Delta^{98}\text{Mo}_{\text{ferrihydrite-seawater}} = \delta^{98}\text{Mo}_{\text{ferrihydrite}} - \delta^{98}\text{Mo}_{\text{seawater}} = -1.1\text{‰}$ ; Goldberg et al., 2009). Under euxinic conditions with  $\text{H}_2\text{S}$  concentrations above  $11\text{ }\mu\text{mol L}^{-1}$  (hereafter called as strongly euxinic conditions), molybdate is almost quantitatively transformed to thiomolybdate ( $\text{MoS}_4^{2-}$ ) (Helz et al., 1996; Nägler et al., 2011), which is readily removed from solution either by adsorption onto organic matter (McManus et al., 2006; Dahl et al., 2010) or by the

formation of authigenic Fe–Mo–sulfides (Helz et al., 2011). As a consequence, the  $\delta^{98}\text{Mo}$  in black shales deposited below such a euxinic water column (hereafter called euxinic sediments) should reflect the isotopic composition of seawater molybdate. Modern euxinic sediments from the Black Sea exhibit the seawater isotopic composition of  $2.3\text{‰}$  (Neubert et al., 2008; Nägler et al., 2011), but are slightly depleted in the heavy isotopes compared to the directly overlying water column, suggesting a small net fractionation between thiomolybdate and authigenic sedimentary Mo of  $\Delta^{98}\text{Mo}_{\text{thiomolybdate-black shale}} = \delta^{98}\text{Mo}_{\text{black shale}} - \delta^{98}\text{Mo}_{\text{thiomolybdate}} = -0.5 \pm 0.3\text{‰}$  (Nägler et al., 2011). This indicates that the removal is only nearly-quantitative even at very high  $\text{H}_2\text{S}$  concentrations. In intermediate redox milieus (e.g., weakly euxinic environments, defined here as environments with low free  $\text{H}_2\text{S}$  concentrations below  $11\text{ }\mu\text{mol L}^{-1}$  and suboxic environments, where  $\text{H}_2\text{S}_{(\text{aq})}$  is only present in the pore-water) the incomplete transformation to thiomolybdate (and the formation of intermediate oxythiomolybdate species  $\text{MoO}_x\text{S}_{4-x}^{2-}$ ) can cause more significant net Mo isotope fractionations. Accordingly, sediments from weakly euxinic depositional environments may reflect almost the full spectrum of observed Mo-isotope variations (Poulson et al., 2006; Siebert et al., 2006; Neubert et al., 2008).

The oxidation of  $\text{Mo}^{4+}$  to  $\text{Mo}^{6+}$  and the formation of soluble molybdate is a prerequisite for large subsequent isotope fractionation. In aqueous environments with Eh higher than  $-0.4\text{ V}$  (at a pH of 8), molybdate is the thermodynamically stable species. By contrast, abiotic oxidation of other redox sensitive metals such as iron ( $\text{Fe}^{2+}$  oxidation to  $\text{Fe}^{3+}$  at Eh of  $-0.1\text{ V}$ ), chromium ( $\text{Cr}^{3+}$  oxidation to  $\text{Cr}^{6+}$  at Eh of  $0.3\text{ V}$ ) or manganese ( $\text{Mn}^{2+}$  oxidation to  $\text{Mn}^{4+}$  at Eh  $> 0.5\text{ V}$ ), need much higher redox potentials (Takeno, 2005). This means that even under very reducing and ferruginous conditions, molybdate remains thermodynamically stable as a dissolved phase in seawater.

The goal of this study is to investigate the onset and mode of Neoproterozoic redox changes in the ocean–atmosphere system. For this purpose we expand the Mo-isotope data of Hamersley Basin sedimentary rocks presented by Duan et al. (2010) back in time, turning our attention to the Mo-isotopic evolution in different Archean sedimentary settings. The distinction between different depositional environments within the same basin throughout the same time interval may provide a more detailed picture of the Neoproterozoic Mo-cycle as well as the evolution of the oceanic redox state at different deposition depths. We present Mo-isotope data from black shales as well as from carbonate and oxide facies iron formations (IF) from the Neoproterozoic Hamersley Basin, spanning a depositional age range of 2.6–2.5 Ga.

## 2. GEOLOGICAL SETTING AND SAMPLE DESCRIPTION

The samples of this study are sedimentary rocks obtained from drill cores ABDP#9 and Millstream#9 from the Hamersley Basin of Western Australia (Fig. 1). Stratigraphically, samples from Millstream#9 represent

the Marra Mamba Iron Formation and the lower part of the Wittenoom Formation, which have an age of  $\sim 2597 \pm 5$  Ma (Fig. 1; Trendall et al., 1998). Samples from ABDP#9 are slightly younger, transitioning from the upper part of the Wittenoom Formation (spherule layer:  $\sim 2541 \pm 18/-15$  Ma; Woodhead et al., 1998) into the Mt. Sylvia Formation, the Mt. McRae Shale ( $\sim 2501 \pm 8$  Ma; Anbar et al., 2007) and the Dales Gorge Member of the Brockman Iron Formation ( $2495 \pm 16$  and  $2461 \pm 6$  Ma; Trendall et al., 2004).

The Hamersley Basin reflects a deep shelf/platform environment below wave base and above the calcite compensation depth (Morris, 1993). Its depositional setting has been described as an outer-shelf environment that was separated from the coast by a carbonate barrier, which inhibited large inputs of terrigenous detrital material (Morris and Horwitz, 1983). The Marra Mamba Iron Formation mainly consists of laminated ferruginous chert and oxide- and carbonate facies iron formation (Klein and Gole, 1981; Krapež et al., 2003) with intercalations of shaly, Fe-rich carbonates (Morris and Horwitz, 1983). The lower Paraburdoo Member of the conformably overlying Wittenoom Formation consists mainly of thinly bedded calcitic/dolomitic/sideritic carbonates. The upper Bee Gorge Member of the Wittenoom Formation represents alternating grey-black shales and limestones/dolostones (Simonson et al., 1993). A several meter thick chert layer, called the Lower Chert, marks the transition to the Mt. Sylvia Formation, which is mainly composed of shales, siliciclastics, and chert units and is capped by a 5 m thick layer of banded iron formation, the so-called Bruno's Band (Krapež et al., 2003). The Mt. McRae Shale consists of two black shale layers (S1 and S2) that are separated by a

Fe-carbonate unit (Anbar et al., 2007). Conformably overlying this is the Dales Gorge Member of the Brockman Iron Formation, which predominantly consists of alternating layers of chert and banded iron formation (Krapež et al., 2003). The metamorphic grade of the Hamersley Basin is sub-greenschist facies (i.e. prehnite-pumpellyite; McConchie, 1984; Anbar et al., 2007).

The samples analyzed for this study include (1) organic rich, black shales, (2) grey-greenish and Fe-rich shaly carbonates, and (3) banded iron formations. Black shales (1) are fine-grained and finely laminated. They show strong enrichments in organic carbon and pyrite, the latter mainly appearing as early diagenetic nodules and disseminated grains. Black shale deposits represent the most proximal setting (Beukes and Gutzmer, 2008). Greenish shale units (2) are also finely laminated. These samples contain less organic carbon and detrital material but are enriched in iron and carbonate. Most samples show disseminated Fe-carbonates in fine-grained chert matrices. Less common are later diagenetic coarse-grained rhombohedral carbonate grains. Beukes and Gutzmer (2008) argue that such samples represent relatively deep marine environments. Iron formations (3) have no detrital material and represent the most distal deep water facies (Beukes and Gutzmer, 2008). These samples show distinct bands of very fine grained chert alternating with bands of reddish hematite and coarse grained, idiomorphic magnetite crystals.

### 3. METHODS

Major element concentrations were determined by X-ray fluorescence analyses (XRF) using the Bruker AXS Pioneer S4 at the University of Tuebingen. Glass beads were

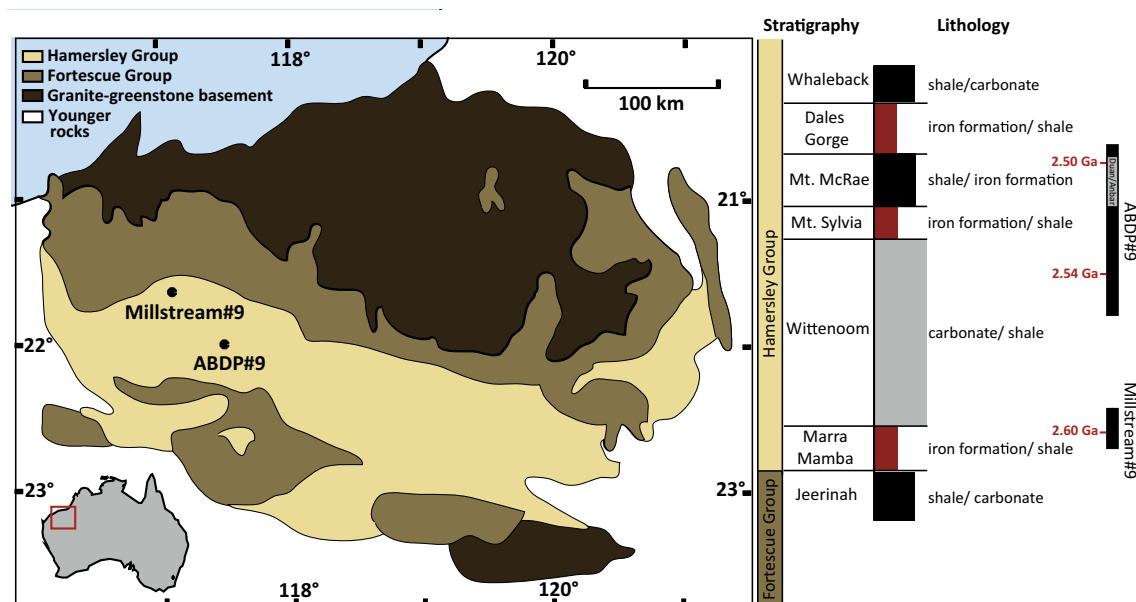


Fig. 1. Geological map of the Pilbara Craton with drill core locations of ABDP#9 and Millstream#9. Also illustrated are the corresponding stratigraphic units and their predominant lithology. The bars on the far right site demonstrate which stratigraphic units are covered by both drill cores of this study and which parts of ABDP#9 were already analyzed by Anbar et al. (2007) and Duan et al. (2010). Also shown are a U-Pb zircon age (2.60 Ga; Trendall et al., 1998), a Pb-Pb age (2.54 Ga; Woodhead et al., 1998), and a Re-Os age (2.50 Ga; Anbar et al., 2007).

prepared by mixing 1.5 g of dried and powdered sample material with 7.5 g lithium tetraborate, which was fused at 1050 °C for 30 min. The loss of ignition was determined on a separate sample aliquot by the weight loss after 60 min of heating in a furnace at 1050 °C. For concentration measurements 32 standardized samples define elemental calibration lines, with element specific analytical uncertainties is element specific (for Fe<sub>2</sub>O<sub>3</sub> the 1 $\sigma$  standard error is 0.0569%).

To determine total organic carbon (TOC), powdered samples were decarbonized with 10% HCl at room temperature and four-times rinsed with ultrapure H<sub>2</sub>O (18.2 M $\Omega$  cm<sup>-1</sup>). This procedure was repeated twice. The concentration of TOC (decarbonized samples) and total carbon (TC; of untreated bulk samples) were then measured by combustion with a Vario elemental analyzer. The total inorganic carbon component (TIC) was calculated as the difference between TC and TOC.

Carbonate carbon and oxygen isotope measurements were determined on bulk sample material that was treated with phosphoric acid (99%) in a He-atmosphere at 90 °C for at least 150 min to fully assure complete dissolution of all carbonates including iron carbonates. Isotopic ratios of the evolving CO<sub>2</sub>-gas were measured by continuous flow with a Gasbench II coupled to a Finnigan MAT 252 gas source mass spectrometer at the University of Tuebingen. Isotope ratios were calibrated with NBS18 ( $\delta^{13}\text{C}$  of -5.00‰ and  $\delta^{18}\text{O}$  of -22.96‰) and NBS19 ( $\delta^{13}\text{C}$  of 1.95‰ and  $\delta^{18}\text{O}$  of -2.20‰ relative to the Vienna Pee Dee Belemnite; V-PDB) and are reported in the  $\delta$ -notation relative to the V-PDB standard:

$$\delta^i X = \left( \frac{\left[ \frac{iX}{jX} \right]_{\text{Sample}}}{\left[ \frac{iX}{jX} \right]_{\text{Standard}}} - 1 \right)$$

where  $X$  is the respective element,  $i$  is the mass of the rare isotope, and  $j$  is the mass of the common isotope.  $\delta$ -values are reported in ‰ by multiplication with a factor of 1000. The external reproducibility is 0.1‰ (2 $\sigma$ ) for both,  $\delta^{13}\text{C}$  and  $\delta^{18}\text{O}$ .

For the determination of the carbon isotopic composition of the organic matter, a few milligrams of the dried and decarbonized sample material were flash combusted at 1050 °C. The evolving CO<sub>2</sub> gas was separated gas-chromatographically with a Carlo Erba NC 2500 elemental analyzer (EA). The EA was coupled to a Finnigan Delta<sup>+</sup>XL for carbon isotope measurements using continuous flow mode. Results were calibrated to the in-house standard USGS 24 and are presented here in the  $\delta$ -notation in per mill and relative to V-PDB.

Mo-isotope analyses follow the method described by Wille et al. (2013). Samples were ashed for 12 h at 600 °C to oxidize organic phases. An adequate amount of a <sup>100</sup>Mo–<sup>97</sup>Mo double spike was added to 50–500 mg powdered sample material prior to sample digestion and Mo-purification. The double-spike method allows for the correction of the instrumental mass bias as well as mass fractionation that might be caused during chromatographic Mo-purification (Rudge et al., 2009). Samples were dissolved in Teflon beakers by sequential digestion steps using

distilled HF, HNO<sub>3</sub> and HCl acids. Mo was purified using a combination of anion and cation exchange chromatography (i.e. using Dowex 1X8, 200–400 mesh and Dowex 50WX8 200–400 mesh resins, respectively) as described by Wille et al. (2013). Molybdenum isotopic ratios were measured on a multi-collector ICP-MS (ThermoFisher Scientific NeptunePlus) at the University of Tuebingen. Measurements of the in-house standard ZH-2, a Mo-rich sulfide that ran through all chemical separation steps, yield a long-term reproducibility on  $\delta^{98}\text{Mo}$  better than 0.09‰ (2 $\sigma$ ). Results were calibrated using the Johnson Matthey ICP standard and are reported in the  $\delta$ -notation relative to the NIST3134 standard (Goldberg et al., 2013), which was set to 0.25‰ following a proposal of Nögler et al. (2014):

$$\delta^{98}\text{Mo} = \left( \frac{\left[ \frac{^{98}\text{Mo}}{^{95}\text{Mo}} \right]_{\text{Sample}}}{\left[ \frac{^{98}\text{Mo}}{^{95}\text{Mo}} \right]_{\text{NIST 3134}}} - 1 \right)$$

#### 4. RESULTS

In order to characterize the set of 23 samples we distinguish petrologically and chemically between black shales, and carbonate and oxide facies iron formations (Table 1). Black shales are rich in TOC, with values between 0.8 and 5.5 weight percent (wt%), have Fe<sub>2</sub>O<sub>3</sub> below 15 wt% and Al<sub>2</sub>O<sub>3</sub> above 10 wt%. In contrast, iron formations have Fe<sub>2</sub>O<sub>3</sub> above 25 wt% and Al<sub>2</sub>O<sub>3</sub> below 5 wt% (and most of them even below 1 wt%). We further distinguish between carbonate and oxide dominated iron formation facies, as well as mixtures of both (carb-IF, ox-IF and carb/ox-IF, respectively). To do so, we calculated the iron formation carbonate fraction assuming that all Ca and Mg are bound in carbonate. We further assumed that all remaining carbonate is ferrous carbonate. All samples with more than 70% of the total iron bound in ferrous carbonate we refer to as carbonate facies iron formation, samples with less than 10% we refer to as oxide facies iron formation, and intermediate samples we refer to as oxide/carbonate facies iron formation. This distinction is confirmed by petrological observations (Fig. 2).

Average concentrations of TIC follow the order ox-IFs (0.8  $\pm$  0.3 wt%) < black shales (1.4  $\pm$  2.2 wt%) < ox/carb IFs (5.9  $\pm$  0.8 wt%) < carb IFs (8.5  $\pm$  1.0 wt%). Corresponding  $\delta^{13}\text{C}_{\text{Carb}}$  values vary strongly (between -17.0‰ and -0.1‰) with averages in the order of black shales (-3.8  $\pm$  3.5‰) > carb IF (-5.6  $\pm$  2.4‰) > ox/carb IFs (-6.9  $\pm$  2.8‰) > ox IFs (-9.7  $\pm$  2.1‰). The  $\delta^{18}\text{O}_{\text{Carb}}$  pattern shows variable values only for black shales (-14.5‰ to -6.7‰) but is homogeneous for all iron formations (-11.1‰ to -9.1‰). For comparison, the oxygen and carbon isotopic composition of 3 limestones (ABDP-260; ABDP-332; ABDP-355) were measured. Both  $\delta^{13}\text{C}_{\text{Carb}}$  and  $\delta^{18}\text{O}_{\text{Carb}}$  values span narrow ranges ( $\delta^{13}\text{C}_{\text{Carb}}$  between -1.27‰ and -0.87‰ and  $\delta^{18}\text{O}_{\text{Carb}}$  between -12.79‰ and -9.04‰). We observe no correlation between  $\delta^{13}\text{C}_{\text{Carb}}$  and  $\delta^{18}\text{O}_{\text{Carb}}$  (Fig. 3). Iron formations show strong variability in  $\delta^{13}\text{C}_{\text{Carb}}$  (with values below limestone  $\delta^{13}\text{C}_{\text{Carb}}$ ) at relatively constant  $\delta^{18}\text{O}_{\text{Carb}}$ .

Table 1  
Main elements of drill cores ABDP#9 and Millstream#9.

Sample	Depth (m)	Formation	Lithology	SiO <sub>2</sub> (wt%)	Al <sub>2</sub> O <sub>3</sub> (wt%)	TiO <sub>2</sub> (wt%)	Fe <sub>2</sub> O <sub>3</sub> (wt%)	MnO (wt%)	MgO (wt%)	CaO (wt%)	Na <sub>2</sub> O (wt%)	K <sub>2</sub> O (wt%)	P <sub>2</sub> O <sub>5</sub> (wt%)	LOI (wt%)	Sum
ABDP-103	102.55	Dales Gorge	carb-IF	12.2	0.0	0.0	53.4	0.2	4.1	1.0	0.0	0.0	0.1	28.0	99.1
ABDP-114	114.4	Mt McRae	black shale	21.9	5.6	0.2	2.9	0.5	11.9	20.4	0.2	2.4	0.0	33.4	99.3
ABDP-133	132.7	Mt McRae	black shale	55.1	11.4	0.4	10.3	0.4	3.6	2.8	0.3	3.2	0.1	10.7	98.4
ABDP-164	163.5	Mt McRae	carb-IF	11.2	4.1	0.1	44.2	0.4	8.4	1.9	0.1	1.5	0.1	29.5	101.4
ABDP-177	176.7	Mt McRae	black shale	56.7	11.9	0.5	9.9	0.1	2.2	0.5	0.5	5.9	0.1	10.5	98.7
ABDP-180	179.8	Mt McRae	carb-IF	32.4	0.6	0.0	30.1	0.7	5.4	5.9	0.0	0.0	0.1	24.4	99.6
ABDP-190	190.2	Mt Sylvia	ox/carb-IF	12.9	0.0	0.0	65.7	0.3	2.7	2.8	0.1	0.0	0.1	15.1	99.6
ABDP-215	214.5	Mt Sylvia	ox-IF	16.4	0.3	0.0	76.3	0.0	2.4	2.1	0.1	0.0	0.1	1.9	99.6
ABDP-219	218.65	Mt Sylvia	black shale	52.0	12.8	0.5	13.3	0.1	3.5	1.3	0.1	6.1	0.1	9.2	98.9
ABDP-220	219.95	Mt Sylvia	ox-IF	58.5	0.0	0.0	37.6	0.0	0.7	1.1	0.1	0.0	0.0	1.0	98.9
ABDP-240	239.5	Wittenoom	black shale	64.8	12.7	0.5	6.8	0.1	3.0	1.3	0.8	3.2	0.0	6.2	99.3
ABDP-259	259.38	Wittenoom	black shale	64.9	10.8	0.4	10.2	0.1	3.4	1.4	0.6	1.4	0.1	5.8	99.3
ABDP-260	259.63	Wittenoom	limestone	9.0	0.1	0.0	1.5	0.6	0.8	48.3	0.1	0.0	0.0	38.6	99.0
ABDP-292	291.6	Wittenoom	carb-IF	22.0	3.6	0.2	28.5	0.4	6.9	11.5	0.1	0.3	0.0	26.2	99.6
ABDP-316	316	Wittenoom	black shale	59.3	16.1	0.6	5.5	0.1	4.2	1.4	3.5	3.6	0.1	4.7	99.2
ABDP-332	332	Wittenoom	limestone	0.9	0.1	0.0	0.8	0.2	0.6	54.8	0.1	0.0	0.0	43.0	100.6
ABDP-335	334.55	Wittenoom	carb-IF	8.6	0.8	0.1	29.3	0.5	6.8	19.3	0.1	0.0	0.1	34.4	99.9
ABDP-340	340	Wittenoom	black shale	57.1	15.9	0.7	6.9	0.2	4.5	2.1	1.3	3.1	0.1	7.5	99.3
ABDP-355	355.18	Wittenoom	limestone	10.7	3.1	0.1	1.7	0.9	1.0	44.4	0.6	0.6	0.0	36.0	99.0
Mill-205	205	Wittenoom	black shale	60.4	16.7	0.6	2.5	0.1	2.5	1.0	0.1	11.4	0.1	4.1	99.4
Mill-206	205.5	Wittenoom	black shale	58.3	13.5	0.7	1.8	0.1	4.1	3.7	0.1	8.2	0.1	8.7	99.3
Mill-217	217	Wittenoom	black shale	59.3	17.7	0.9	1.9	0.0	2.6	0.4	0.1	10.7	0.1	5.6	99.2
Mill-223	223	Marra Mamba	carb-IF	6.5	1.1	0.1	35.1	0.8	9.7	13.9	0.0	0.0	0.1	32.8	100.1
Mill-223.2	223.2	Marra Mamba	carb-IF	7.8	1.8	0.1	26.8	0.8	10.5	17.7	0.1	0.2	0.1	33.5	99.5
Mill-225	225	Marra Mamba	ox/carb-IF	12.3	1.1	0.1	40.5	0.6	6.9	15.1	0.2	0.4	0.1	22.4	99.6
Mill-229	229.3	Marra Mamba	black shale	45.8	11.0	0.5	2.6	0.3	7.6	9.2	0.1	6.0	0.1	16.3	99.5



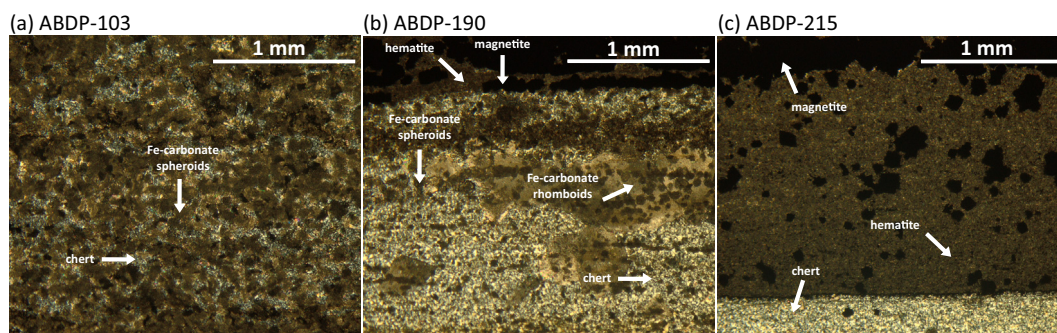


Fig. 2. Reflected light microscopy images of samples ABDP-103 (a), ABDP-190 (b) and ABDP-215 (c). (a) Shows iron carbonate spheroids in a fine grained chert matrix. Iron carbonate rhombs and iron carbonate spheroids within chert are observed in (b). A layer of fine grained hematite and large magnetite crystals marks a distinct boundary. (c) Shows a fine chert matrix separated from a thick band of hematite filled with magnetite crystals.

Average TOC contents increase in the order ox-IFs ( $0.1 \pm 0.0$  wt%) = ox/carb-IFs ( $0.1 \pm 0.1$  wt%) < carb-IFs ( $0.7 \pm 0.4$  wt%) < black shales ( $2.4 \pm 1.5$  wt%). The corresponding  $\delta^{13}\text{C}_{\text{Org}}$  values vary between  $-43.3\text{‰}$  and  $-27.2\text{‰}$  with averages of carb IFs ( $-35.9 \pm 4.9\text{‰}$ ), black shales ( $-33.6 \pm 3.0\text{‰}$ ), ox/carb-IFs ( $-32.5 \pm 5.3\text{‰}$ ) and ox-IFs ( $-30.1 \pm 1.9\text{‰}$ ) (Table 2). Considering only black shale samples,  $\delta^{13}\text{C}_{\text{Carb}}$  and  $\delta^{13}\text{C}_{\text{Org}}$  exhibit a positive linear correlation with an  $R^2$  value of 0.86, whereas no correlation is observed in both types of iron formations (Fig. 3b). Accordingly, the difference in  $\delta^{13}\text{C}_{\text{Org}}$  and  $\delta^{13}\text{C}_{\text{Carb}}$  ( $\Delta^{13}\text{C}_{\text{Org-carb}}$ ) is  $-29.85 \pm 1.36\text{‰}$  and very constant in black shales, but varies strongly in IFs ( $-26.15 \pm 8.45\text{‰}$ ).

For the determination of authigenic molybdenum concentrations, we corrected all samples for a detrital component by normalizing on Al, assuming that all Al is detrital with a chemical composition of the Post Archean Australian Shale (PAAS) (Taylor and McLennan, 1985). Al concentrations in iron formations are very low and show only weak correlation with Mo concentrations ( $R^2$  of 0.39; Fig. 4a), which clearly does not match the range of Al/Mo ratios of average continental crust. The correction further indicates that more than 80% of Mo in iron formations is non-detrital, but authigenic (see Table 2). Black shales have higher Al concentrations but are also enriched in Mo. The relative proportion of authigenic Mo is always above 77% (mostly even above 85%). Mo and Al show no correlation and suggest that Mo enrichment was decoupled from the detrital input.

Authigenic Mo concentrations vary between 0.3 and 13 ppm and averages increase in the order ox-IFs ( $0.4 \pm 0.1$   $\mu\text{g/g}$ ) = carb/ox-IFs ( $0.4 \pm 0.1$   $\mu\text{g/g}$ ) < carb-IFs ( $0.8 \pm 0.4$   $\mu\text{g/g}$ ) < black shales ( $7.1 \pm 8.9$   $\mu\text{g/g}$ ; Table 2). Considering only black shales, we observe average authigenic Mo concentrations of 2.2  $\mu\text{g/g}$  in the Marra Mamba Formation (1 sample),  $3.3 \pm 1.2$   $\mu\text{g/g}$  in the Wittenoom Formation (7 samples), 3.8  $\mu\text{g/g}$  in the Mt. Sylvia Formation (1 sample),  $3.9 \pm 1.3$   $\mu\text{g/g}$  in the S2 of the Mt. McRae Shale (19 samples; this study and Anbar et al., 2007) and  $18.5 \pm 9.4$   $\mu\text{g/g}$  in the S1 layer of the Mt. McRae Shale (46 samples; Anbar et al., 2007 and this study) revealing a concentration increase with time. Mo concentrations in all sedimentary rocks show no correlation

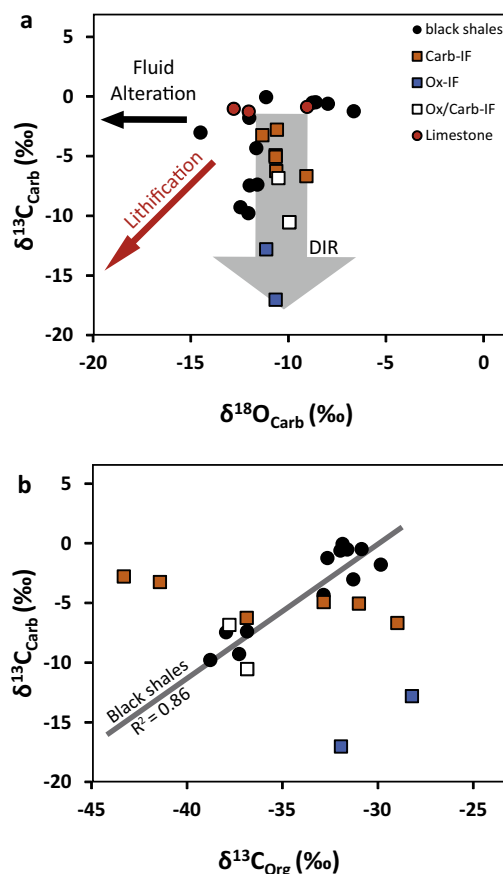


Fig. 3. (a) Compilation of  $\delta^{18}\text{O}$  and  $\delta^{13}\text{C}$  of carbonates in bulk rock samples. Expected trends for fluid alteration or lithification during diagenesis (Knauth and Kennedy, 2009) are not observed. Iron formations have generally lower  $\delta^{13}\text{C}_{\text{Carb}}$  but similar  $\delta^{18}\text{O}_{\text{Carb}}$  as limestones (red circles), which is the result of iron carbonate formation during dissimilatory iron reduction (DIR); (b) Illustrates  $\delta^{13}\text{C}_{\text{Org}}$  vs.  $\delta^{13}\text{C}_{\text{Carb}}$  showing a correlation only in black shale samples (black circles). Iron formations, displayed as squares (orange: carbonate facies IFs, white: oxide/carbonate facies IFs, blue: oxide facies IFs), exhibit no correlation. (For interpretation of the references to color in this figure legend, the reader is referred to the web version of this article.)

Table 2  
Selected geochemical parameters of drill cores ABDP#9 and Millstream#9.

Sample	Depth (m)	Formation	Lithology	TOC (wt%)	TIC (wt%)	TC (wt%)	$\delta^{18}\text{O}_{\text{Carb}}$ †† ‰	$\delta^{13}\text{C}_{\text{Carb}}$ †† ‰	$\delta^{13}\text{C}_{\text{Org}}$ †† ‰	$\Delta^{13}\text{C}$ ‰	$\delta^{98}\text{Mo}$ ‰	2SE abs	Mo μg/g	Mo* μg/g	Mo*/TOC (μg/g/wt%)
ABDP-103	102.55	Dales Gorge	carb-IF	0.6	8.2	8.3	−9.07	−6.69	−28.98	−22.28	1.51	0.03	1.4	1.4	2.3
ABDP-114	114.4	Mt McRae	black shale	3.3	8.0	11.4	−6.65	−1.23	−32.64	−31.42	1.31	0.02	4.0	3.7	1.1
ABDP-133	132.7	Mt McRae	black shale	4.7	0.8	5.4	−12.45	−9.28	−37.27	−27.99	1.37	0.01	13.7	13.1	2.8
ABDP-164	163.5	Mt McRae	carb-IF	1.4	8.3	9.7	−10.62	−6.26	−36.87	−30.61	1.05	0.02	1.4	1.1	0.8
ABDP-177	176.7	Mt McRae	black shale	5.5	0.2	5.7	−12.05	−9.79	−38.78	−28.99	0.97	0.02	3.5	2.9	0.6
ABDP-180	179.8	Mt McRae	carb-IF	0.4	7.1	7.6	−9.95	−10.54	−36.84	−26.30	0.92	0.04	0.2	0.2	0.4
ABDP-190	190.2	Mt Sylvia	ox/carb-IF	0.0	5.1	5.1	−10.98	−12.52	−27.23	−14.70	0.90	0.05	0.5	0.5	12.5
ABDP-215	214.5	Mt Sylvia	ox-IF	0.1	1.1	1.2	−11.13	−12.81	−28.21	−15.40	0.83	0.04	0.3	0.3	4.5
ABDP-219	218.65	Mt Sylvia	black shale	3.6	0.6	4.2	−11.98	−7.46	−37.95	−30.49	1.10	0.02	4.5	3.8	1.0
ABDP-220	219.95	Mt Sylvia	ox-IF	0.1	0.6	0.6	−10.65	−17.03	−31.93	−14.90	0.64	0.05	0.4	0.4	6.9
ABDP-240	239.5	Wittenoom	black shale	1.4	0.4	1.8	−11.59	−7.37	−36.85	−29.48	0.58	0.03	2.1	1.4	1.0
ABDP-259	259.38	Wittenoom	black shale	1.1	0.5	1.6	−11.64	−4.32	−32.84	−28.53	0.89	0.03	2.5	1.9	1.8
ABDP-292	291.6	Wittenoom	carb-IF	0.5	7.1	7.6	−11.32	−4.94	−32.84	−27.90	0.72	0.03	1.2	1.0	2.1
ABDP-316	316	Wittenoom	black shale	1.0	0.3	1.3	−14.50	−3.02	−31.29	−28.27	0.61	0.02	4.4	3.6	3.7
ABDP-335	334.55	Wittenoom	carb-IF	0.2	9.9	10.1	−10.58	−5.05	−30.99	−25.94	0.57	0.12	0.6	0.5	2.9
ABDP-340	340	Wittenoom	black shale	2.0	0.5	2.5	−12.00	−1.78	−29.84	−28.06	0.62	0.02	3.8	2.9	1.5
Mill-205	205	Wittenoom	black shale	1.8	0.3	2.1	−7.98	−0.60	−31.96	−31.36	0.52	0.02	4.1	3.5	1.9
Mill-206	205.5	Wittenoom	black shale	1.7	1.4	3.1	−11.14	−0.05	−31.85	−31.80	0.84	0.01	4.9	4.2	2.5
Mill-217	217	Wittenoom	black shale	2.5	0.1	2.4	−8.60	−0.48	−30.85	−30.37	0.79	0.03	6.2	5.3	2.1
Mill-223	223	Marra Mamba	carb-IF	0.6	9.3	9.9	−9.82	−2.78	−43.31	−40.52	0.72	0.03	0.4	0.3	0.5
Mill-223.2	223.2	Marra Mamba	carb-IF	1.1	9.3	10.3	−10.07	−3.26	−41.41	−38.15	1.51	0.02	0.9	0.8	0.7
Mill-225	225	Marra Mamba	ox/carb-IF	0.2	6.8	6.9	−10.51	−6.85	−37.77	−30.92	0.51	0.03	0.4	0.3	2.0
Mill-229	229.3	Marra Mamba	black shale	0.8	3.8	4.6	−8.77	−0.53	−31.60	−31.08	0.59	0.02	2.8	2.2	2.9

\* Authigenic Mo concentrations corrected for the detrital input.

†† Relative to V-PDB.

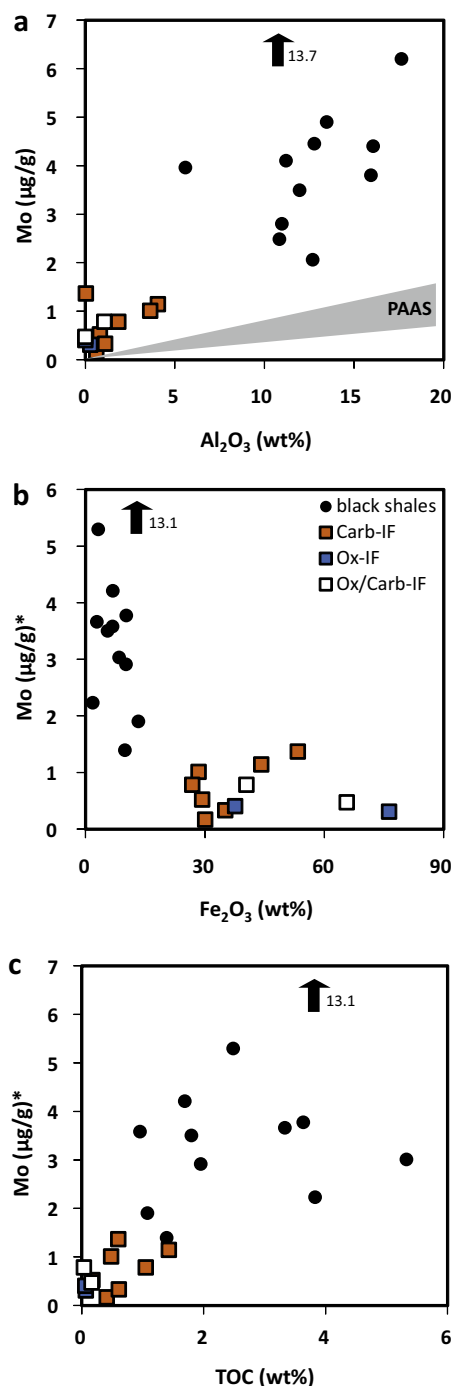


Fig. 4. Molybdenum concentration vs.  $\text{Al}_2\text{O}_3$  (a),  $\text{Fe}_2\text{O}_3$  (b) and TOC (c) concentrations, respectively. Note that authigenic molybdenum concentrations were plotted in (b) and (c) as indicated by \*. Symbols are as in Fig. 3. Grey shading indicates the expected range for samples with predominantly detrital Mo (PAAS: Post Archean Australian Shale) Taylor and McLennan (1985). (For interpretation of the references to color in this figure legend, the reader is referred to the web version of this article.)

with iron (Fig. 4b) but a positive correlation with TOC (Fig. 4c). Excluding the one black shale outlier with extremely high Mo and TOC, the linear trend between Mo

and TOC has an  $R^2$  value of 0.51. Mo/TOC ratios of black shales are between 1.0 and 3.7 ppm/wt% and show no correlation with the molybdenum isotopic composition ( $\delta^{98}\text{Mo}$ ). The  $\delta^{98}\text{Mo}$  values are between +0.51‰ and +1.51‰ (Fig. 5) and thus above the  $\delta^{98}\text{Mo}$  composition of the continental crust. Black shales and carb-IFs of similar core depth have a similar Mo-isotopic composition (i.e. compare sample pairs ABDP-177 and ABDP-180, ABDP-335 and ABDP-340, and Mill-225 and Mill-229, respectively; Table 2). Oxide-IFs show more negative  $\delta^{98}\text{Mo}$  values compared to black shales of similar core depth ( $\Delta^{98}\text{Mo}_{\text{Ox-IF-black shale}} = \delta^{98}\text{Mo}_{\text{Ox-IF}} - \delta^{98}\text{Mo}_{\text{black shale}} = -0.4\text{‰}$ ). Independent of the sediment type we observe a general increase in  $\delta^{98}\text{Mo}$  of up to 1.51‰ passing up stratigraphy through the Mt. Sylvia Formation, Mt. McRae Shale and Brockman Iron Formation (Fig. 5). By contrast, older sedimentary rocks of the Marra Mamba and Wittenoom formations exhibit lower  $\delta^{98}\text{Mo}$ , at a relatively constant level (mean of  $0.66 \pm 0.24\text{‰}$  ( $2\sigma$ ); excluding the outlier Millstream-223.2). Age constraints of a spherule layer within the Bee Gorge Member in drill core ABDP#9 (observed at a core depth of 295 m) define the onset of this increase in  $\delta^{98}\text{Mo}$  to an age slightly younger than 2.54 Ga (Woodhead et al., 1998).

## 5. DISCUSSION

The environmental conditions during sedimentation are critical for the removal mechanism of molybdate from the water column. As our samples span very different depositional settings across the continental shelf/slope, a more detailed analysis of prevailing environmental conditions is necessary.

### 5.1. Black shales

Black shales were deposited in a distal shelf environment, an area with relatively high primary microbial productivity and high detrital input. On average the detrital fraction accounts for 62 wt% of the black shales, assuming that all Al and Ti originate from detritus with a chemical composition of PAAS. However, less than 25% of sedimentary Mo (usually even less than 15%) is detrital, indicating strong authigenic Mo enrichment. High TOC contents up to 5.5 wt% are consistent with deposition in an anoxic environment. In more detail, we observe that black shales with high TOC (Mt. McRae Shale) have generally low  $\delta^{13}\text{C}_{\text{Org}}$  (down to  $-38.8\text{‰}$  in ABDP-177) as well as low  $\delta^{13}\text{C}_{\text{Carb}}$  (down to  $-9.8\text{‰}$  in ABDP-177; Figs. 3 and 5). Nearly constant  $\Delta^{13}\text{C}_{\text{Org-Carb}}$  values of  $-29.85 \pm 1.36\text{‰}$  mirror the expected range of fractionation during primary production in the Neoproterozoic (Eigenbrode and Freeman, 2006). The tight coupling of  $\delta^{13}\text{C}_{\text{Org}}$  and  $\delta^{13}\text{C}_{\text{Carb}}$  suggests one single carbon source for carbonates and organic matter, namely dissolved inorganic carbon (DIC) of the ambient seawater, which changed in its isotopic composition over time. This could indicate global trends with elevated  $\delta^{13}\text{C}_{\text{DIC}}$ ,  $\delta^{13}\text{C}_{\text{Org}}$  and  $\delta^{13}\text{C}_{\text{Carb}}$  during periods of high organic matter burial rates. However, such a correlation was not observed in contemporaneous sedimentary rocks of the Griqualand



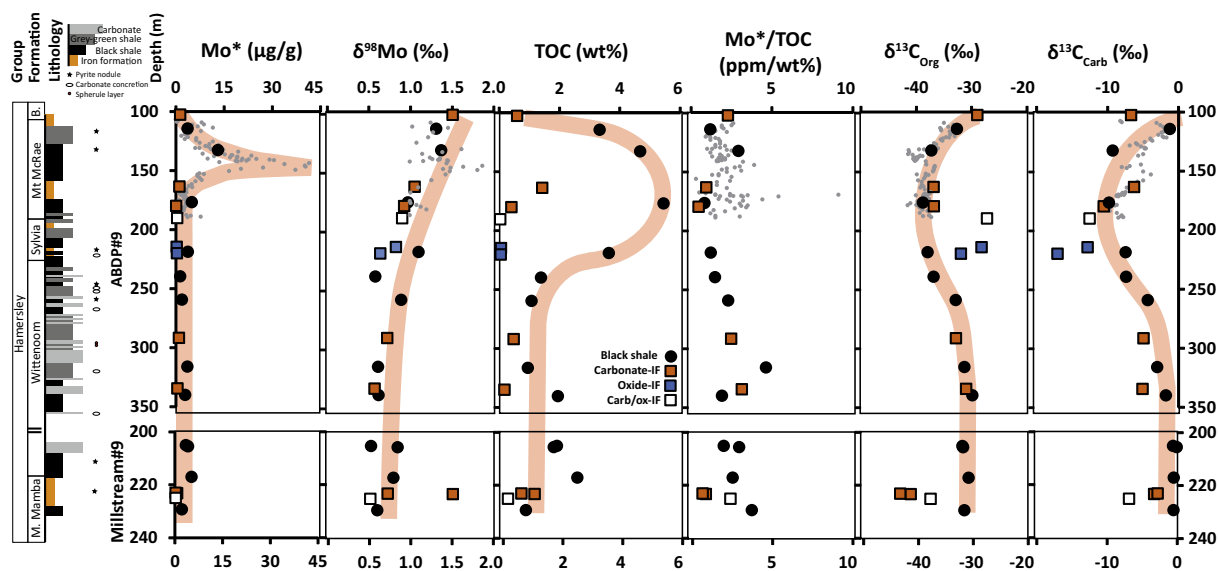


Fig. 5. Geochemical parameters including authigenic  $\text{Mo}^*$  concentration,  $\delta^{98}\text{Mo}$ , TOC,  $\text{Mo}^*/\text{TOC}$ ,  $\delta^{13}\text{C}_{\text{Org}}$  and  $\delta^{13}\text{C}_{\text{Carb}}$  vs. core depth of ABDP#9 and Millstream#9, respectively. Symbols are as in Fig. 3. Small grey dots indicate higher resolution data from Anbar et al. (2007), Duan et al. (2010), and Kaufman et al. (2007). Red lines illustrate trends in black shale samples only, which are broadly confirmed by higher resolution data. (For interpretation of the references to color in this figure legend, the reader is referred to the web version of this article.)

West Basin, South Africa (Fischer et al., 2009). Considering the consistently higher  $\delta^{13}\text{C}_{\text{Carb}}$  values of shallower water limestones ( $-1.27\text{‰}$  to  $-0.87\text{‰}$  in  $\delta^{13}\text{C}_{\text{Carb}}$ ), a more plausible explanation for this feature is a local shelf environment that was characterized by a stratified water column with a large gradient (up to  $9\text{‰}$ ) in the  $\delta^{13}\text{C}_{\text{DIC}}$  (Jiang et al., 2007). Periods of low  $\delta^{13}\text{C}_{\text{Org}}$ , low  $\delta^{13}\text{C}_{\text{Carb}}$  and high TOC could reflect the upwelling of nutrient rich deep waters that were depleted in  $^{13}\text{C}$  (Kaufman et al., 1991; Jiang et al., 2007). Such environmental conditions stimulate primary production (high TOC), as well as the activity of heterotrophic organisms. Productivity of methanogenic bacteria appears to be subordinate, as the expected difference in  $\delta^{13}\text{C}_{\text{Org}}$  and  $\delta^{13}\text{C}_{\text{Carb}}$  would be much larger. However, organisms that reduce sulfate and elemental sulfur within the sediment were very common throughout the Neoproterozoic Hamersley Group deposition (Partridge et al., 2008), as is also indicated by the abundance of diagenetic pyrite in our black shales. Locally formed euxinic conditions in the water column and/or the sediment would cause molybdate transformation to oxythiomolybdate ( $\text{MoO}_x\text{S}_{4-x}^{2-}$ ) and/or thiomolybdate depending on the ambient concentration of dissolved  $\text{H}_2\text{S}_{(\text{aq})}$  (Helz et al., 1996; Neubert et al., 2008; Nägler et al., 2011). At  $\text{H}_2\text{S}_{(\text{aq})}$  concentrations above  $11\text{ }\mu\text{mol L}^{-1}$ , thiomolybdate ( $\text{MoS}_4^{2-}$ ) is the predominant species with a maximum abundance of 83% (Erickson and Helz, 2000; Nägler et al., 2011) and with a constant Mo isotope fractionation between sediment and thiomolybdate of  $\Delta^{98}\text{Mo}_{\text{MoS}_4\text{-sediment}} = -0.5 \pm 0.3\text{‰}$  (Nägler et al., 2011). Assuming that the remaining 17% represent the  $\text{MoOS}_3^{2-}$  species with  $\Delta^{98}\text{Mo}_{\text{MoOS}_3\text{-MoS}_4}$  of  $-1.75\text{‰}$  (Nägler et al., 2011), the equilibrium fractionation between the sediment and euxinic seawater with  $\text{H}_2\text{S}_{(\text{aq})}$  above  $11\text{ }\mu\text{mol L}^{-1}$  is  $\Delta^{98}\text{Mo}_{\text{euxinic\_seawater-sediment}} \approx -0.7\text{‰}$ ,

consistent with observations in the Black Sea (Neubert et al., 2008; Nägler et al., 2011). Only if the removal is nearly quantitative (as in the deep Black Sea, where dissolved Mo-concentrations drop down to  $8\text{ nmol L}^{-1}$  compared to  $105\text{ nmol L}^{-1}$  in the open ocean; Algeo and Lyons, 2006) the isotopic composition of the sediment mirrors that of global seawater (Fig. 6). However, sedimentary  $\delta^{98}\text{Mo}$  might be up to  $0.7\text{‰}$  lower compared to the  $\delta^{98}\text{Mo}$  of global seawater, if the removal is non-quantitative (Fig. 6). In the case of the Cariaco Basin, Mo-removal from seawater is clearly non-quantitative, as indicated by only slightly lower concentrations of dissolved Mo ( $\sim 80\text{ nmol L}^{-1}$ ) compared to the global ocean ( $105\text{ nmol L}^{-1}$ ) (Algeo and Lyons, 2006). This might be due to lower  $\text{H}_2\text{S}_{(\text{aq})}$  concentrations, which are slightly below the switching point within the water column and unknown for the pore-water, and/or due to larger seawater exchange rates (Algeo and Lyons, 2006). The  $\delta^{98}\text{Mo}$  value of sediments from the Cariaco Basin deposited around 13 ka ago (Lyons et al., 2003) is around  $0.5\text{‰}$  lower than the modern global seawater isotopic composition (Fig. 6) (Arnold et al., 2004). Although the environmental conditions might have changed during the last 13 ka (e.g.  $\text{H}_2\text{S}_{(\text{aq})}$  concentration and water renewal times), this may additionally indicate that basinal restriction is a key parameter that controls seawater Mo depletion and the preservation of the seawater Mo isotopic composition. If this model is correct, the deep water within the Cariaco Basin should show  $\delta^{98}\text{Mo}$  slightly above the global seawater  $\delta^{98}\text{Mo}$ . We therefore note that the  $\delta^{98}\text{Mo}$  of ancient sediments only reflects the seawater  $\delta^{98}\text{Mo}$  when  $\text{H}_2\text{S}_{(\text{aq})}$  concentrations of the seawater or pore-water were above  $11\text{ }\mu\text{mol L}^{-1}$  (Erickson and Helz, 2000; Neubert et al., 2008) and when the marine depositional setting was connected to the open

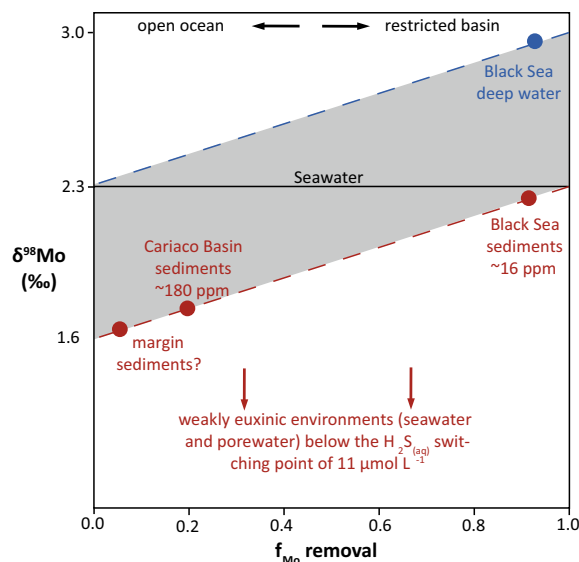


Fig. 6. The hypothetical equilibrium isotope fractionation between euxinic seawater (*Black Sea*; Neubert et al., 2008) and possibly pore-water (e.g. *Cariaco Basin*; Arnold et al., 2004; and continental margins; Poulson et al. (2006) and Poulson Brucker et al. (2009)) with  $H_2S_{(aq)}$  above  $11 \mu\text{mol L}^{-1}$  (blue) and underlying sediments (red) in dependence of the Mo-fraction that is removed from seawater. We assume maximal thiomolybdate formation of 83%, the rest being  $\text{MoOS}_3^{2-}$  Erickson and Helz (2000) and Nägler et al. (2011), giving an equilibrium isotope fractionation of  $\sim -0.7\text{‰}$  in  $\delta^{98}\text{Mo}$  Nägler et al. (2011). In weakly euxinic environments with  $H_2S_{(aq)}$  below  $11 \mu\text{mol L}^{-1}$ , when thiomolybdate formation is less predominant, significantly larger fractionations are possible. (For interpretation of the references to color in this figure legend, the reader is referred to the web version of this article.)

ocean but restricted enough to allow quantitative removal (Algeo and Lyons, 2006). If the removal of Mo is non-quantitative (like in the *Cariaco Basin*), sediments in euxinic settings are up to  $0.7\text{‰}$  lower in  $\delta^{98}\text{Mo}$  than the ambient seawater.

In non-euxinic marine settings (e.g. suboxic settings with low bottom water  $O_2$  and  $H_2S_{(aq)} < 5 \mu\text{mol L}^{-1}$  and  $<< 10 \mu\text{mol L}^{-1}$ , or ferruginous settings with no bottom water  $H_2S_{(aq)}$  and  $O_2$ ) the mechanisms of Mo-sequestration are different (Scott and Lyons, 2012). In these intermediate redox environments, Mo is scavenged from pore-water molybdate that can derive from seawater through diffusion, from reductive dissolution of Fe–Mn oxides in the uppermost layers of the sediment (Reitz et al., 2007; Scott and Lyons, 2012), or from decomposition of organic matter (Dellwig et al., 2007; Poulson Brucker et al., 2009; Kowalski et al., 2013). Mn-oxides, the predominant Mo-adsorbent in the modern oxic oceans, do not form inorganically below an Eh of 0.5 V at a marine pH of 8. Therefore, the role of Mn oxides might be subordinate in a largely anoxic Archean environment, although some studies point to local Mn oxide formation in iron formations already before the GOE (Crowe et al., 2013; Planavsky et al., 2014). We observe very low Mn concentrations and no correlation in Fe/Mn with  $\delta^{98}\text{Mo}$  like Planavsky et al. (2014), which indicates that Mn oxide formation and re-dissolution within

the sediment was unimportant in the black shale setting of the Hamersley Basin. Fe oxides were possibly present but probably more important in iron formation settings (see Sections 5.2 and 5.3). Relative Fe-depletion along with Mo enrichment in black shales excludes that the adsorption on Fe-oxyhydroxides was the predominant removal mechanism. In non-euxinic black shale settings, the diffusion of seawater molybdate into the sediments and the demineralisation of organic matter were probably the predominant sources of pore-water molybdate (Fig. 7).

Mo associated with organic matter is adsorbed onto organic aggregates or incorporated into the cells or both. The incorporation into cells can (but does not have to) cause a coordination change from tetrahedral to octahedral depending on the specific incorporation mechanism (see Liermann et al., 2005 for more details). Expected Mo-isotope fractionations during this coordination change were confirmed during experiments, although fractionation magnitudes are relatively low and range from  $\Delta^{98}\text{Mo}_{\text{organic cells-seawater}} = \delta^{98}\text{Mo}_{\text{organic cells}} - \delta^{98}\text{Mo}_{\text{seawater}} = -0.2\text{‰}$  to  $-1\text{‰}$  (Nägler et al., 2004; Liermann et al., 2005; Zerkle et al., 2011). However, this effect might be subordinate, because the cells of nitrogen fixing cyanobacteria, which use Mo-rich enzymes, have only low Mo concentrations between 0.2 and 2.4 ppm (Tuit et al., 2004). The relative contribution of cell related Mo to the total authigenic Mo fraction is very low (on average only  $1.3 \pm 0.6\%$  in our black shale samples assuming the high-end cell-Mo concentration of 2.4 ppm). This might indicate that the adsorption of molybdate onto organic aggregates dominates, a process that is associated with low Mo-isotope fractionations (Kowalski et al., 2013). The pore-water molybdate in non-euxinic black shale settings therefore likely has a similar Mo-isotopic composition as seawater. It is transformed to oxythiomolybdate and/or thiomolybdate and scavenged by sulfurized organic matter, if a zone of sulfate reduction prevailed within the sediment (Fig. 7) (Helz et al., 1996; Tribouillard et al., 2004; Poulson et al., 2006; Scott and Lyons, 2012). Such a zone is indicated by the abundance of early diagenetic pyrite in our black shales. As described above, the magnitude of Mo-isotope fractionation during this process is mainly dependent on the ambient  $H_2S_{(aq)}$  concentration within the sediment. In open marine settings with ferruginous bottom waters and high pore-water  $H_2S_{(aq)}$  concentrations the Mo isotopic composition of the sediments is very uniform and close to the seawater Mo isotopic composition with  $\Delta^{98}\text{Mo}_{\text{ferruginous sediment-seawater}} = \delta^{98}\text{Mo}_{\text{ferruginous sediment}} - \delta^{98}\text{Mo}_{\text{seawater}} = -0.7\text{‰}$  (Poulson et al., 2006; Poulson Brucker et al., 2009). Interestingly, this fractionation magnitude is expected for an open marine setting with quantitative thiomolybdate formation assuming the equilibrium fractionation model (Fig. 6), but such an interpretation is speculative and requires further investigation. However, variability in the  $\delta^{98}\text{Mo}$  of anoxic margin sediments is only expected if (1) the seawater  $\delta^{98}\text{Mo}$  changes, (2) the reductive dissolution of Fe–Mn oxides is relevant, or (3) thiomolybdate formation is non-quantitative ( $H_2S_{(aq)} < 11 \mu\text{mol L}^{-1}$ ). For example, in suboxic settings where the reductive dissolution of Fe–Mn oxides is relevant, this

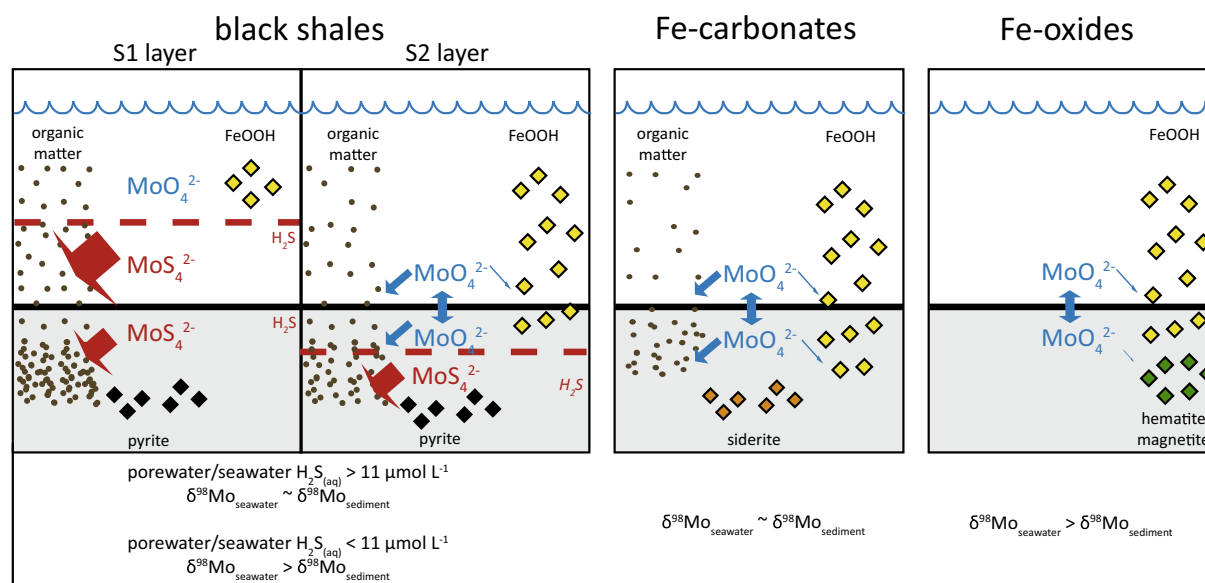


Fig. 7. Simplified box model for Mo sequestration in black shale, Fe-carbonate and Fe-oxide settings. In black shale settings Mo is scavenged by sulfurized organic matter in a sulfidic zone in the water column (S1 layer) or within the sediment (S2 layer). In Fe-carbonate settings the adsorption of molybdate onto organic matter is the predominant Mo-removal pathway, whereas the adsorption onto Fe-oxyhydroxides is of minor importance. By contrast, in Fe-oxide settings where the supply of organic matter is largely missing, this adsorption mechanism becomes more important. Mo sequestration increases in the order Fe oxides < Fe-carbonates < “ferruginous” black shales (S2) < “euxinic” black shales (S1). Mo isotope fractionations in black shales are low, as long as H<sub>2</sub>S<sub>(aq)</sub> concentrations within the water column and the sediment, respectively, are above the switching point of 11 μmol L<sup>-1</sup>. Also the adsorption onto organic matter, the predominant Mo-removal pathway in Fe-carbonates is associated with low Mo isotope fractionations, so that the δ<sup>98</sup>Mo of black shales and Fe-carbonates might be similarly close to the δ<sup>98</sup>Mo of ancient seawater. In Fe-oxide settings isotopically light Mo is preferentially adsorbed onto Fe-oxyhydroxides and/or hematite/magnetite, which causes slightly lower δ<sup>98</sup>Mo in Fe-oxides compared to nearly contemporaneous black shales.

additional source for pore-water molybdate can cause a larger range in the sedimentary Mo-isotopic composition of suboxic margin sediments (Siebert et al., 2006). The same would be true if thiomolybdate formation is incomplete, as occurs in weakly euxinic sedimentary environments.

Fe-speciation is commonly used to classify local redox conditions and to distinguish between euxinic and non-euxinic settings (Raiswell and Canfield, 1998; Poulton et al., 2004). However, we note that the distinction between weakly and strongly euxinic depositional environments of ancient sedimentary rocks is difficult, even with Fe speciation data. This proxy gives no exact indication about the quantitative H<sub>2</sub>S concentration and hence whether the switching point of 11 μmol L<sup>-1</sup> H<sub>2</sub>S was reached and thiomolybdate formation was nearly quantitative or not. Therefore, even black shales with iron speciation data indicating a euxinic depositional environment may not fully imprint the ambient seawater’s Mo-isotopic composition. Moreover, the Fe speciation data refer to the water column redox state (Poulton et al., 2004). Efficient Mo-scavenging within the sulfate reduction zone of the sediment can still be the predominant removal pathway even if the overlying water column is ferruginous (e.g. see Poulton et al., 2006). Reinhard et al. (2009) showed that the ambient seawater during the deposition of the S2 layer of the Mt. McRae Shale was mainly ferruginous, whereas it was mainly euxinic during deposition of the younger S1 layer. We measured the Mo isotopic composition of two black shales from S1 (ABDP-114, ABDP-133) and one black shale from

S2 (ABDP-177). Despite lower resolution, like Duan et al. (2010) we observe slightly lower δ<sup>98</sup>Mo in the older and non-euxinic S2 layer and even lower values in black shales from older formations, an observation that can be explained by two different scenarios:

- (1) Consistent with the Fe-speciation data of Reinhard et al. (2009), the increase could indicate the preferential removal of light Mo isotopes in non-euxinic settings like the S2 layer, whereas the euxinic S1 layer might mimic the Neoproterozoic seawater Mo isotopic composition (Duan et al., 2010). Even if we exclude the reductive dissolution of Mn-oxides at our black shale depositional settings, weakly euxinic conditions in the pore-water of S2 with H<sub>2</sub>S<sub>(aq)</sub> concentrations below the switching point of 11 μmol L<sup>-1</sup> could have caused large Mo-isotope differences between seawater and sediment (Neubert et al., 2008). The continuous increase from low δ<sup>98</sup>Mo during the Marra Mamba and Wittenoom black shales towards highest values in the S1 layer could indicate that Mo-isotope fractionations became less pronounced, possibly due to increasing pore-water H<sub>2</sub>S<sub>(aq)</sub> concentrations. In this scenario the seawater Mo-isotopic composition could have remained relatively constant with δ<sup>98</sup>Mo as high as those observed in the strongly euxinic S1 layer, which would give the best approximation for the ancient seawater δ<sup>98</sup>Mo (Duan et al., 2010).

(2) Alternatively, our data would indicate a temporal increase in seawater  $\delta^{98}\text{Mo}$ , whereas authigenic molybdenum enrichment in the black shales remained quantitative and thus mirrored the changing seawater  $\delta^{98}\text{Mo}$  (Duan et al., 2010). We prefer this scenario to the previous one for several reasons that will be discussed below, as well as in chapters 5.2 and 5.3. Considering the good correlation of Mo and TOC, Mo scavenging by sulfurized organic matter seems a reasonable removal pathway (Tribouillard et al., 2004) (Fig. 7). The large abundance of diagenetic pyrite indicates that  $\text{H}_2\text{S}$  and bacterial sulfate reduction prevailed within the sediment also during S2 deposition and deposition of older black shales (Reinhard et al., 2009). If thiomolybdate formation in this zone was nearly quantitative, all black shales (below a ferruginous and sulfidic water column) will show  $\delta^{98}\text{Mo}$  that are similarly close to, and reflect minimum values of, the  $\delta^{98}\text{Mo}$  of ancient seawater. We admit that the assumption of quantitative thiomolybdate formation remains hypothetical. However, we would expect large scatter in our  $\delta^{98}\text{Mo}$  dataset if pore-water  $\text{H}_2\text{S}_{(\text{aq})}$  concentrations were relatively low and variable. Such scattering in  $\delta^{98}\text{Mo}$  values is observed in contemporaneous black shales of the Griqualand West Basin, South Africa (Wille et al., 2007). Consistent with less efficient Mo-removal in weakly euxinic environments, Mo concentrations in the black shales of this location are also significantly lower (Wille et al., 2007). The lack of such pronounced scatter in our  $\delta^{98}\text{Mo}$  dataset from the Hamersley Basin with continuously increasing values argues against strongly variable authigenic enrichment factors under fluctuating low  $\text{H}_2\text{S}$  concentrations. We therefore suggest that the best modern analogue for our black shale settings are anoxic margin settings, where Mn-cycling is negligible, the seawater–sediment interface is ferruginous (and was only partly euxinic as during S1 deposition) and a sulfidic zone formed in the sulfate reduction zone within the sediment (Poulson et al., 2006; Poulson Brucker et al., 2009). These sediments, where pore-water molybdate was effectively scavenged by formation of oxythiomolybdate and organic matter deposition, exhibit relatively small Mo isotopic differences between seawater and sediments (Poulson et al., 2006; Scott and Lyons, 2012). The main difference to a hypothetical Neoproterozoic analogue was a significantly smaller seawater Mo-reservoir, as indicated by continuously low Mo/TOC (Scott et al., 2008). Quantitative Mo removal is easier achieved at such low seawater molybdate concentrations (Duan et al., 2010), such that Archean sediments may even more closely reflect the seawater  $\delta^{98}\text{Mo}$  (Fig. 6). Mo enrichments will be highest when the bottom water was also euxinic, as during deposition of the S1 layer, but lower when the supply of molybdate is mainly dependent on the diffusional transport of seawater molybdate into the sediment. This might

explain the extreme Mo enrichments in the black shales of S1 (Reinhard et al., 2009).

We conclude that during black shale deposition, the sediment and the sediment–water interface were anoxic and partly euxinic (S1, Mt. McRae Shale; Reinhard et al., 2009). The Mo-isotope data of authigenic Mo in these black shales reflect minimum values for ambient seawater (Wille et al., 2007). The continuous increase in black shale  $\delta^{98}\text{Mo}$  from a mean value of  $0.66\text{‰} \pm 0.22$  ( $2\sigma$ ) before 2.54 Ga up to  $1.37\text{‰}$  in the Mt. McRae Shale could therefore indicate decreasing net Mo scavenging in the youngest samples or (as preferred here) an increase in the Mo-isotopic composition of the ambient seawater.

## 5.2. Carbonate facies iron formation

Carb-IFs formed on the shelf/slope in more distal and deeper environments than black shales (Beukes and Gutzmer, 2008). The detrital influence during deposition of these units was negligible, as indicated by low Al and Ti concentrations (Table 1). Fe-carbonates precipitate when a solution is oversaturated in  $\text{Fe}^{2+}$  and  $\text{HCO}_3^-$  (Beukes et al., 1990; Winter and Knauth, 1992). Ohmoto et al. (2004) suggested that such oversaturation in Archean seawater was a consequence of extremely high atmospheric  $p(\text{CO}_2)$ . However, a more recent study of the  $^{87}\text{Rb}$ – $^{87}\text{Sr}$  radiogenic isotope system in iron carbonates points to an early diagenetic origin of Archean iron carbonates (Johnson et al., 2013). The oxidation of organic matter and coupled dissimilatory iron reduction during early diagenesis can also create an oversaturation of  $\text{Fe}^{2+}$  and  $\text{HCO}_3^-$  within the sediment's pore-water (Ellwood et al., 1988; Johnson et al., 2008) and the subsequent precipitation of iron carbonates before lithification (Johnson et al., 2013). This formation mechanism is consistent with lower  $\delta^{13}\text{C}_{\text{carb}}$  in carb-IFs compared to limestones, as it strongly indicates the integration of isotopically light carbon that was derived from organic matter remineralization within the sediment (Fig. 3a). Furthermore, the spheroidal shape of iron carbonate investigated in this study (Fig. 2a and b) was most likely caused by the reaction of ferrihydrite with organic matter during early diagenesis (Köhler et al., 2013). Ferrihydrite, which is the presumed precursor mineral for any iron formation, can form during iron oxidation by photoferrotrophic bacteria (Widdel et al., 1993) or inorganically by free oxygen in an oxic ocean surface layer (Cloud, 1965), whereas photo oxidation was ruled out as primary mechanism for Fe-oxidation and subsequent BIF formation (Konhauser et al., 2007). The spheroidal and rhombohedral shape of iron carbonates might indicate that photoferrotrophic bacteria were the predominant primary producer (Köhler et al., 2013). The subsequent oxidation of organic matter by  $\text{Fe}^{3+}$  within the sediment requires the absence of energetically more efficient oxidants such as  $\text{O}_2$ . Furthermore, reduced iron would preferentially form iron sulfides if  $\text{H}_2\text{S}$  was available (Poulton et al., 2004). Consequently, iron carbonates formed in an anoxic and non-sulfidic pore-water environment overlain



by a ferruginous water column (Poulton et al., 2004; Holland, 2006; Kaufman et al., 2007).

In an  $H_2S$  free pore-water/seawater environment, the formation and scavenging of thiomolybdate is excluded. Furthermore, the role of Mn-oxides and hence the adsorption of molybdate onto these minerals was probably of minor importance in an anoxic environment (see one exception in Section 5.4). Still, Fe-carbonates are enriched in authigenic Mo, which make up more than 80% of total Mo (Table 2). Considering the genesis of Fe-carbonates, molybdenum was either scavenged by organic matter or by Fe-oxyhydroxides. We would expect similar Mo enrichments in oxide and carbonate facies iron formations, if the adsorption onto Fe-oxyhydroxides was the predominant scavenging mechanism. However, authigenic Mo concentrations increase in the order oxide IF < carb/ox IF < carb IF. Thereby, authigenic Mo concentrations positively correlate with TOC. This rather suggests that Mo scavenging by organic matter was the predominant process (Fig. 7), a mechanism that was shown to be very efficient in the modern German Wadden Sea (Dellwig et al., 2007; Kowalski et al., 2013). It appears that only in settings with very low organic carbon burial rates does the adsorption of molybdate onto Fe-(oxyhydr)oxides significantly contribute to the sequestration of Mo into the sediments (Wichard et al., 2009).

The concentrations of Mo are lower in Fe carbonates compared to black shales, because a sulfidic zone and thiomolybdate formation was absent (Fig. 7). Independent of all these different Mo enrichment mechanisms, we observe very similar  $\delta^{98}Mo$  values in black shale/carbonate IF sample pairs APDB-177/APDB-180, APDB-335/APDB-340, and Mill-225/Mill-229, which are similar in depth and probably age (Table 2; Fig. 5). Furthermore, the  $\delta^{98}Mo$  values of Fe carbonates generally follow the same trend as the  $\delta^{98}Mo$  values of black shales with highest values in the youngest samples (excluding sample Mill-223.2, see Section 5.4; Fig. 5). Considering the low Mo-isotope fractionations during Mo-scavenging by organic matter (Kowalski et al., 2013), the increase in  $\delta^{98}Mo$  values of Fe-carbonates in the course of the Mt. Sylvia Formation, Mt. McRae Shale and Brockman Iron Formation indicates an increase in the seawater  $\delta^{98}Mo$ . This in turn confirms our previous hypothesis that the magnitude of Mo scavenging in all black shale samples was similar and nearly quantitative, probably due to nearly quantitative thiomolybdate formation in  $H_2S$  rich sedimentary settings. Therefore, the most straightforward interpretation of the  $\delta^{98}Mo$  record suggests similarly small Mo isotopic differences between seawater and black shales as well as carbonate facies iron formations, respectively, and an increase in the seawater  $\delta^{98}Mo$  over the course of the deposition of the Mt. Sylvia Formation, Mt. McRae Shale and Brockman Iron Formation.

### 5.3. Oxide facies iron formation

According to Beukes and Gutzmer (2008), oxide-IFs represent the most distal deep-water facies in an anoxic environment. Correspondingly, the respective samples show

no detrital component (undetectable concentrations of Al and Ti). Furthermore, TOC concentrations are extremely low (in the range of the analytical detection limit). Low TOC might limit the coupled reaction of iron (III) reduction and organic matter oxidation and hence the formation of iron carbonates. By contrast, the labile Fe-oxyhydroxide fraction formed layers of iron oxides such as hematite and magnetite during early diagenesis (Fig. 2b and c; Beukes and Gutzmer, 2008). Some samples show both, iron carbonates and iron oxides (Fig. 2b). The thin section in Fig. 2b clearly demonstrates the separation of iron carbonate and iron oxide layers, which suggests continuous sediment deposition under changing environmental conditions. The absence of pyrite in both types of iron formations indicates a ferruginous and non-sulfidic environment during deposition.

Oxide facies iron formations, as with carbonate facies iron formations, reveal a large authigenic Mo component. The  $H_2S$  free environment in these settings impedes the formation of particle reactive thiomolybdate and subsequent Mo sequestration as is the case for Fe carbonate settings. But, opposite to Fe carbonate settings, we suggest that the burial rate of organic matter was low enough so that Mo adsorption onto Fe-oxyhydroxides was the predominant authigenic Mo enrichment process in oxide facies iron formations (Fig. 7). This adsorption causes Mo-isotopic differences of  $\Delta^{98}Mo_{\text{ferrihydrite-seawater}} = \delta^{98}Mo_{\text{ferrihydrite}} - \delta^{98}Mo_{\text{seawater}}$  of  $-1.1\text{‰}$  (Goldberg et al., 2009). Consistent with our hypothesis the  $\delta^{98}Mo$  of two pure oxide IFs (ABDP-215 and ABDP-220) are slightly lower than the  $\delta^{98}Mo$  of the “contemporaneous” black shale (ABDP-219;  $\Delta^{98}Mo_{\text{ABDP215/220-ABDP219}} = \delta^{98}Mo_{\text{ABDP215/220}} - \delta^{98}Mo_{\text{ABDP219}} = -0.4\text{‰}$ ; Table 2). Low Mo concentrations in Fe oxides suggest that the efficiency of Mo removal at these settings was generally low, which could have been a question of competition for free adsorption sites. The Archean ocean was rich in Si (with concentrations more than 60 times higher than today; Siever, 1992), which has a higher affinity to ferric (oxyhydr)oxides than Mo (Balistrieri and Chao, 1990). During times of non-biological Si precipitation, mineral adsorption represented the main Si removal mechanism in the Archean ocean (Siever, 1992). Thus, the chemical composition of the Archean ocean (i.e. high Si concentrations), might have significantly hindered Mo-adsorption on ferric (oxyhydr)oxides.

### 5.4. The evolution of seawater $\delta^{98}Mo$

The continental crust (and hence detrital Mo) has a relatively narrow range in  $\delta^{98}Mo$  values between  $0.0\text{‰}$  and  $0.6\text{‰}$ , with an average continental  $\delta^{98}Mo$  value of ca.  $0.3\text{--}0.4\text{‰}$  (Greber et al., 2014; Siebert et al., 2003; Wille et al., 2013; Voegelin et al., 2014). Most early and middle Archean sedimentary rocks exhibit  $\delta^{98}Mo$  values within this continental range (Siebert et al., 2005; Wille et al., 2013; Voegelin et al., 2014) along with low Mo/TOC ratios (Scott et al., 2008; Wille et al., 2013). Some higher  $\delta^{98}Mo$  values in  $\sim 3.0$  Ga old iron formations, which positively correlate with Fe/Mn ratios, point to local Mo-isotope fractionations during adsorption onto Mn-oxides (Planavsky



et al., 2014). Altogether the current dataset suggests low seawater Mo concentrations (low Mo/TOC) along with global inhomogeneity of Archean seawater  $\delta^{98}\text{Mo}$ , with temporal and spatial variability being dependent on the local Mo input as well as local fractionation processes (e.g. Planavsky et al., 2014).

The sedimentary rocks from the Neoproterozoic Marra Mamba and Wittenoom formations, Hamersley Basin, exhibit authigenic Mo enrichment, but still low Mo/TOC ratios. Most  $\delta^{98}\text{Mo}$  values are only slightly above the average value of the continental crust and close to the majority of early and middle Archean  $\delta^{98}\text{Mo}$  values, which indicates unchanged environmental conditions. One exception (Fe carbonate Mill-223.2) shows an anomalously high  $\delta^{98}\text{Mo}$  value of 1.51‰ that is in stark contrast to significantly lower  $\delta^{98}\text{Mo}$  values of all other samples of the Marra Mamba and Wittenoom formations. In addition, the carbonate IF (Mill-223), which is only 20 cm above this sample, has a significantly lower  $\delta^{98}\text{Mo}$  value of 0.72‰. The geochemical, petrological and mineralogical similarity of both Fe carbonates argues against a different Mo removal mechanism with variable Mo-isotope fractionations. Such

short-term variability could result from the local formation of Mn-oxides. Mn-oxides represent an impermanent sink for isotopically light Mo (Scott and Lyons, 2012). During reductive dissolution of Mn-oxides within the sediment Mo is re-liberated and diffuses back into the water column as long as it is not fixed within a sulfidic zone of the sediment (Scott and Lyons, 2012). This means that isotopically light Mo is only temporary bound as long as Mn-oxides persist in the uppermost sediment layers and could temporary cause high  $\delta^{98}\text{Mo}$  values of local seawater (i.e. during deposition of Mill-223.2). Theoretically, later instability of local Mn oxides in more reducing environments would re-liberate isotopically light Mo shifting the local seawater  $\delta^{98}\text{Mo}$  back to lower values (i.e. during deposition of Mill-223). Such short scale temporal variability is only imaginable when the reservoir size of seawater molybdate is small and its residence time is short (consistent with low Mo/TOC ratios).

Alternatively, temporary high  $\delta^{98}\text{Mo}$  values could also reflect a short-term increase of a homogeneous  $\delta^{98}\text{Mo}_{\text{sw}}$  reservoir, which might also explain similarly high  $\delta^{98}\text{Mo}$  values observed in nearly contemporaneous carbonates on

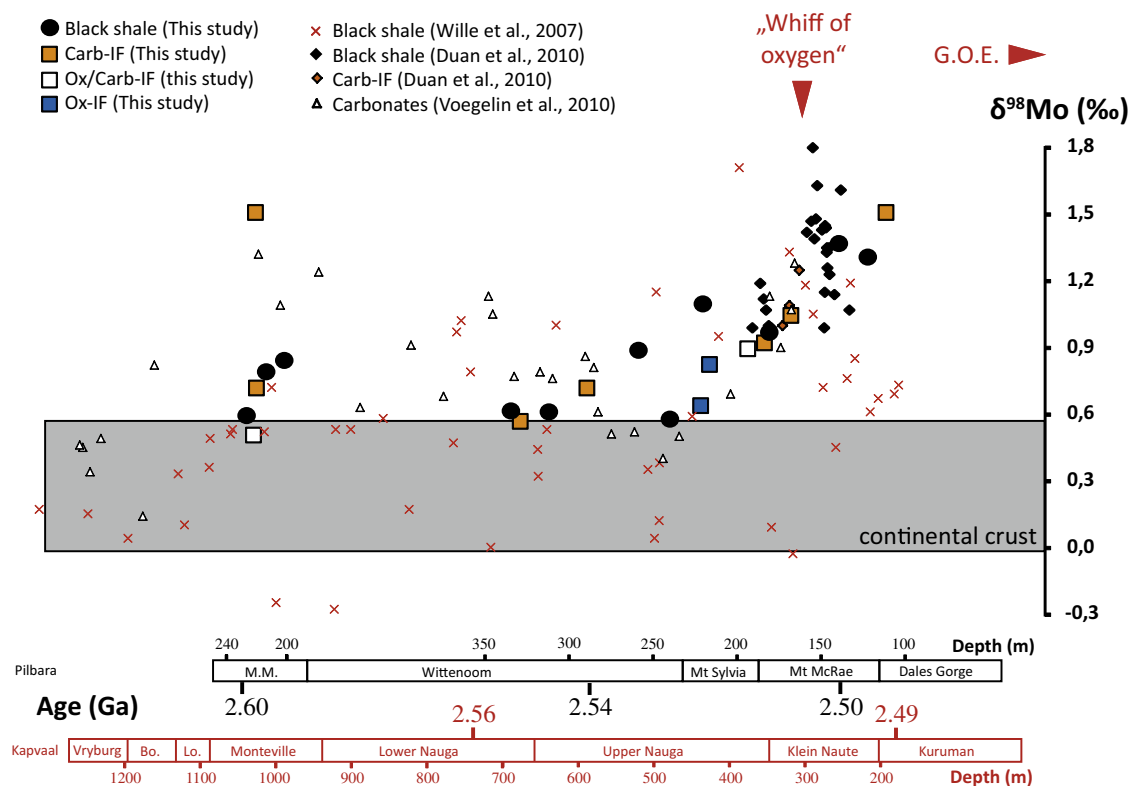


Fig. 8. The evolution of  $\delta^{98}\text{Mo}$  in black shales, carbonates and iron formations during the Neoproterozoic (Hamersley Basin: Duan et al., 2010 and this study; Griqualand West Basin: Wille et al., 2007; Voegelin et al., 2010). The  $\delta^{98}\text{Mo}$  are plotted against sample depth of the Australian drill cores ABDP#9 and Millstream#9 (black: Duan et al., 2010; this study) and the Australian drill core GKP01 (red: Wille et al., 2007; Voegelin et al., 2010). All sample sets were time-correlated using spherule layers (Simonson et al., 2009), U-Pb zircon ages (2.60 Ga; Trendall et al., 1998), Pb-Pb ages (2.54 Ga; Woodhead et al., 1998) and a Re-Os shale age (2.50 Ga; Anbar et al., 2007). Our data show low  $\delta^{98}\text{Mo}$  close to crustal values (grey area) before 2.54 Ga (Marra Mamba and Wittenoom formation) and a subsequent increase towards more positive values (Mt. Sylvia Formation, Mt. McRae Shale and Brockman Formation). Samples from the Griqualand West Basin, South Africa, (Wille et al., 2007) show larger variability but a qualitatively similar trend in maximum values. The increase is concomitant for black shales (black circles) and carbonate facies iron formation (orange squares). Ultimately, the increase is attributed to the build-up of a more homogeneous oceanic molybdate reservoir with a higher seawater  $\delta^{98}\text{Mo}$  as a consequence of increasing redox-potentials before the G.O.E. and the "whiff" of oxygen. (For interpretation of the references to color in this figure legend, the reader is referred to the web version of this article.)

the Kapvaal craton (Fig. 8) (Voegelin et al., 2010). Assuming such homogeneous distribution of Mo in seawater, we used the box-model described in Wille et al. (2008) to model the effect of an abruptly larger sink of isotopically light Mo on the seawater Mo isotopic composition (spike on the left in panel 2, Fig. 9a). Similarly, we modeled the effects of an abrupt short-term increase in the Mo-influx and the Mo removal efficiency, respectively, on the  $\delta^{98}\text{Mo}_{\text{sw}}$  values (abrupt doubling for 100 ka at constant isotopic differences between seawater and sediment; spike on the left in panel 1, Fig. 9b and c, respectively). The seawater Mo inventory was set to 1% of the modern inventory (Scott et al., 2008). Reduced oxidative weathering on the continents during the Archean are expected to cause a significantly lower Mo-influx, which we also set to 1% of the modern influx (=outflux in steady state). Although Neoarchean Mo-fluxes are poorly constrained and the resulting modern-like residence time might be overvalued, we note that the perturbation of the Mo ocean inventory and its isotopic composition depend on changing the relative proportions of the two fluxes and the inventory as well as their isotopic compositions. The choice of these parameters assures homogenous seawater Mo distribution. The Mo-isotopic composition of the influx was kept constant at 0.4‰ in  $\delta^{98}\text{Mo}$  throughout all models (Voegelin et al., 2014). For simplicity, we assume only two outfluxes. The euxinic outflux comprises 15% of the total outflux (Scott et al., 2008) with a Mo-isotopic composition, which equals that of seawater. For the remaining 85% of outflux in mainly reducing but not strongly euxinic environments an isotopic difference of  $\Delta^{98}\text{Mo}_{\text{sw-sed}} = \delta^{98}\text{Mo}_{\text{sw}} - \delta^{98}\text{Mo}_{\text{sed}} = 0.9\text{‰}$  in steady state (Kendall et al., 2009) is assumed. We note that an increase in  $\Delta^{98}\text{Mo}_{\text{sw-sed}}$  models the relative extension of weakly sulfidic as well as oxic environments, both of which will remove isotopically light Mo. The temporal increase of this value on the 10th to 100th ka timescale can explain short-term variability of seawater  $\delta^{98}\text{Mo}$  (left side in panel 3, Fig. 9a) only if the period of perturbation gets closer to the range of the seawater residence time of Mo (~700 ka in the modern ocean and in the models). The short-term variability of  $\delta^{98}\text{Mo}_{\text{sw}}$  is, however, amplified when combining higher  $\Delta^{98}\text{Mo}_{\text{sw-sed}}$  with an abrupt increase in Mo removal efficiency (left side in panel 3, Fig. 9d). Such a combination is expected during increased Mo scavenging in more widespread weakly euxinic settings and better explains temporally high  $\delta^{98}\text{Mo}_{\text{sw}}$  values as seen in the Marra Mamba formation. However, during periods of strong Mo removal we would expect Mo enrichments and high – rather than low – Mo/TOC ratios during times of increased Mo removal efficiency (Wille et al., 2008). So far such enrichments are not observed in the global geological record. We therefore prefer the initial interpretation that the exceptional increase towards a high  $\delta^{98}\text{Mo}$  value at 2.6 Ga (e.g. in Mill-223.2) is a local phenomenon, which is consistent with a seawater Mo-reservoir that was still heterogeneous and variable with respect to its isotopic composition.

In contrast to mainly low  $\delta^{98}\text{Mo}$  values close to the crustal average in sediments of the Marra Mamba and Wittenoom formations with only one single excursion to

higher values, we observe continuously increasing  $\delta^{98}\text{Mo}$  values in the samples younger than 2.54 Ga, belonging to the Mt. Sylvia Formation, the Mt. McRae Shale and the Dales Gorge Member of the Brockman Iron Formation (ABDP-260 to –102; Fig. 8). The Neoarchean increase in  $\delta^{98}\text{Mo}$  values of Hamersley Basin sedimentary rocks (up to 1.51‰ here and up to 1.86‰ for the S1 layer in the Mt. McRae Shale; Duan et al., 2010) was also observed in contemporaneous sedimentary rocks of the Griqualand West Basin, South Africa (Wille et al., 2007; Voegelin et al., 2010). The large scatter in black shales from the Griqualand West Basin (Wille et al., 2007) could be a consequence of Mo-isotope fractionations in weakly sulfidic settings or mixing of detrital and authigenic Mo (see Section 5.1). However, maximum values, which represent the best approximation for the ancient seawater  $\delta^{98}\text{Mo}$ , show a broadly similar evolution (Fig. 8). These observations suggest that the seawater became isotopically heavier and more homogeneous with respect to Mo, at least regionally within the basin that straddled the South African and Australian regions.

Mo/TOC ratios remained relatively low also during deposition of the Mt. Sylvia Formation and the Mt. McRae Shale, which seems at odds with a larger and more homogeneous seawater Mo reservoir. However, the magnitude of Mo/TOC ratios is also dependent on local environmental conditions such as sedimentation rates and particularly sulfide levels (Algeo and Lyons, 2006; Dahl et al., 2013). Comparing the Mo/TOC ratios from the euxinic S1 interval of the Mt. McRae Shale ( $\text{Fe}_{\text{HR}}/\text{Fe}_{\text{T}} > 0.38$  and  $\text{Fe}_{\text{Py}}/\text{Fe}_{\text{HR}} > 0.8$ ; Reinhard et al., 2009) with Mo/TOC ratios from a euxinic interval of the 2.66 Ga old Jeerinah Formation of the conformably underlying Fortescue Group, Western Australia ( $\text{Fe}_{\text{HR}}/\text{Fe}_{\text{T}} > 0.38$  and  $\text{Fe}_{\text{Py}}/\text{Fe}_{\text{HR}} > 0.8$ ; Scott et al., 2011), the increase in Mo/TOC ratios from averaged  $0.4 \pm 0.2$  in Jeerinah black shales (Scott et al., 2011) to averaged  $2.0 \pm 0.6$  in Hamersley Basin Mt. McRae black shales (Anbar et al., 2007) is significant. First strong enrichment of Mo in euxinic black shales of the Mt. McRae Shale, which led to the idea of a whiff of oxygen before the G.O.E. (Anbar et al., 2007) are therefore consistent with a larger and more homogeneous seawater Mo reservoir. These Mo enrichments required euxinic seawater conditions that could have been a consequence of local oceanographic changes (e.g. the upwelling of DIC and nutrient rich deep waters). Such local oceanographic changes in turn led to strong variations in the carbon isotope record but had little effects on the Mo-isotopic composition. The  $\delta^{98}\text{Mo}$  still increases during the Dales Gorge Member, whereas the  $\delta^{13}\text{C}_{\text{org}}$  and  $\delta^{13}\text{C}_{\text{carb}}$  shift back to lower values (see red lines in Fig. 5). This pattern additionally suggests that the seawater molybdate reservoir was less affected by local changes but rather more homogeneous in its distribution and isotopic composition. Thus, the increase in the seawater molybdate reservoir apparently goes hand in hand with higher seawater  $\delta^{98}\text{Mo}$ .

The possible causes for the build-up of a more homogeneous and isotopically heavier ocean are well discussed by Duan et al. (2010). These authors exclude a hydrothermal



Fe-oxyhydroxides. The sequestration of isotopically light Mo in oxide facies iron formations with only slightly lower  $\delta^{98}\text{Mo}$  values also appear to have been subordinate, considering the extremely low Mo concentrations of oxide IFs. Duan et al. (2010) conclude instead that the preferential removal of isotopically light Mo onto Mn oxides either during oxidative weathering on the continents or in well oxygenated marine coastal areas was a more probable cause. The generation of continental crust coupled with considerable relief-building increased remarkably during the Neoproterozoic (Flament et al., 2008; Rey and Coltice, 2008). Higher reliefs would have increased rates of physical weathering and the riverine and aeolian input of detrital material. In the course of increasing atmospheric oxygen concentrations (Anbar et al., 2007), higher rates of oxidative weathering are expected. Mn oxide formation and the involved retention of isotopically light Mo in well oxygenated surface ocean areas possibly caused higher seawater  $\delta^{98}\text{Mo}$  values (Duan et al., 2010). This idea is confirmed by our modeling. The smooth long-term increase (over 40 Ma) of the Mo-influx by higher rates of oxidative weathering increases the Mo-inventory consistent with higher Mo concentrations and increasing Mo/TOC ratios in the Mt. McRae Shale. However, this increase alone cannot explain the shift towards higher seawater  $\delta^{98}\text{Mo}$  (right side in panel 3, Fig. 9b). Also the long-term increase in Mo removal efficiency has little effects on the  $\delta^{98}\text{Mo}_{\text{sw}}$  (right side in panel 3, Fig. 9c). However, by coupling a higher Mo-influx with higher  $\Delta^{98}\text{Mo}_{\text{sw-sed}}$  (i.e. due to Mo-adsorption onto Mn-oxides), our model suggests a significant and long-term increase in the  $\delta^{98}\text{Mo}_{\text{sw}}$  as well as the seawater Mo inventory consistent with the observed geological record (right side in panel 3, Fig. 9e). We therefore agree with Duan et al. (2010) that the increasing presence of Mn-oxides on well oxygenated shelf regions could have caused continuously higher  $\delta^{98}\text{Mo}$  in black shales and siderites as long as the seawater Mo reservoir was at least regionally homogeneous.

Alternatively, light Mo was preferentially removed in weakly sulfidic environments, which would have similar effects on the  $\delta^{98}\text{Mo}_{\text{sw}}$ . Coevally with increasing oxygenation in the course of the GOE, the weathering of sulfides on the continents led to elevated fluxes of sulfate and molybdenum to the oceans. On the one hand, this could have increased the ocean's Mo inventory and thus be a possible explanation for its more homogeneous distribution. On the other hand, higher sulfate concentrations stimulated bacterial sulfate reduction and hence the formation of sulfidic conditions (Reinhard et al., 2009). Thereby the build-up of a larger Mo inventory requires a Mo influx, which outbalances higher Mo removal rates in weakly euxinic settings. A larger inventory and more euxinic conditions enabled large Mo enrichments in black shales (Anbar et al., 2007). In the very beginning of environmental oxygenation before the GOE, the development of more weakly sulfidic rather than strongly conditions might be favored, which could have caused the gradual increase in the seawater  $\delta^{98}\text{Mo}$  during the Neoproterozoic. For example, the predominant formation of  $\text{MoO}_3\text{S}^{2-}$  rather than

$\text{MoS}_4^{2-}$  in environments with  $\text{H}_2\text{S}_{(\text{aq})}$  concentrations lower than  $5 \mu\text{mol L}^{-1}$  cause large fractionations up to 3‰ in  $\delta^{98}\text{Mo}$  (Neubert et al., 2008) and possibly the build-up of an isotopically heavy ocean. The subsequent areal expansion of sulfidic conditions during further oxygenation in the course and after the GOE could have caused the development of more strongly sulfidic conditions with  $\text{H}_2\text{S}_{(\text{aq})}$  concentrations above  $11 \mu\text{mol L}^{-1}$  and reduced net Mo-isotope fractionations (Duan et al., 2010). This could explain the leveling down of seawater  $\delta^{98}\text{Mo}$  during the Proterozoic (Arnold et al., 2004; Kendall et al., 2009; Duan et al., 2010).

## 6. CONCLUSIONS

The molybdenum isotopic composition of black shales and carbonate facies iron formations exhibit authigenic Mo enrichment with near “crustal”  $\delta^{98}\text{Mo}$  values in the Marra Mamba and Wittenoom formations (2.6–2.54 Ga) of the Hamersley Group, Western Australia, with only one single exception with significantly higher  $\delta^{98}\text{Mo}$ . These results suggest a small and inhomogeneous seawater molybdate reservoir that was dominated by the unfractionated continental Mo input. Fractionation processes on Mn-oxides were temporally and spatially restricted causing locally high seawater  $\delta^{98}\text{Mo}$ . Passing up section through the Mt. Sylvia Formation, Mt. McRae Shale and the Brockman Iron Formation  $\delta^{98}\text{Mo}$  values continuously increase over time (2.54–2.50 Ga), by up to 1.5‰. We suggest that the uniform increase in  $\delta^{98}\text{Mo}$  in Fe carbonates and black shales along with a good correlation of Mo concentration with total organic carbon, is best explained by two removal mechanisms that are associated with similarly low Mo-isotope fractionations, e.g. the adsorption of molybdate onto organic matter in Fe carbonate settings and thiomolybdate scavenging by the formation of sulfurized organic matter in the euxinic pore-water environments of black shale settings. Only in oxide iron formation settings does the adsorption of Mo onto Fe-oxyhydroxides seem relevant. Consistent with new modeling presented here, the concomitant increase in  $\delta^{98}\text{Mo}$  within shelf sediments of the Hamersley Basin, Australia, and the Griqualand West Basin, South Africa, implies the build-up of a homogeneous and isotopically heavy Mo seawater reservoir after 2.54 Ga. The larger Mo reservoir size could have been a consequence of higher Mo-fluxes during oxidative weathering on the continents. The formation of Mn oxides during weathering or within well oxygenated coastal areas could have caused a seawater molybdate reservoir with high  $\delta^{98}\text{Mo}$ . In contrast, iron formation appear to be unsuitable as an important sink for isotopically light Mo. Alternatively, the formation of weakly sulfidic conditions during early stages of environmental oxygenation could have amplified the sequestration of isotopically light Mo. Both explanations require mild oxygenation and sulfide weathering on the continents already before the GOE, so that our results and interpretations are in line with previous studies.



## ACKNOWLEDGEMENTS

We are grateful for the technical support by Bernd Steinhilber and Elmar Reitter. We acknowledge financial support by the Carl Zeiss Foundation, Germany, and by grant WI3870/2-1 from the German Research Foundation (DFG). MVK was supported by the University of New South Wales, Australia. This is contribution 632 from the ARC Centre of Excellence for Core to Crust Fluid Systems (<http://www.ccfcs.mq.edu.au>). We further thank three anonymous reviewers for their helpful and constructive comments.

## REFERENCES

- Algeo T. J. and Lyons T. W. (2006) Mo–total organic carbon covariation in modern anoxic marine environments: Implications for analysis of paleoredox and paleohydrographic conditions. *Paleoceanography*, 21.
- Anbar A. D., Duan Y., Lyons T. W., Arnold G. L., Kendall B., Creaser R. A., Kaufman A. J., Gordon G. W., Scott C., Garvin J. and Buick R. (2007) A whiff of oxygen before the great oxidation event? *Science* **317**, 1903–1906.
- Arnold G. L., Anbar A., Barling J. and Lyons T. (2004) Molybdenum isotope evidence for widespread anoxia in mid-Proterozoic oceans. *Science* **304**, 87–90.
- Balistrieri L. S. and Chao T. (1990) Adsorption of selenium by amorphous iron oxyhydroxide and manganese dioxide. *Geochim. Cosmochim. Acta* **54**, 739–751.
- Barling J., Arnold G. L. and Anbar A. (2001) Natural mass-dependent variations in the isotopic composition of molybdenum. *Earth Planet. Sci. Lett.* **193**, 447–457.
- Bekker A., Holland H., Wang P.-L., Rumble D., Stein H., Hannah J., Coetzee L. and Beukes N. (2004) Dating the rise of atmospheric oxygen. *Nature* **427**, 117–120.
- Beukes N. J. and Gutzmer J. (2008) Origin and paleoenvironmental significance of major iron formations at the Archean–Paleoproterozoic boundary. *Rev. Econ. Geol.* **15**, 5–47.
- Beukes N. J., Klein C., Kaufman A. J. and Hayes J. (1990) Carbonate petrography, kerogen distribution, and carbon and oxygen isotope variations in an early Proterozoic transition from limestone to iron-formation deposition, Transvaal Supergroup, South Africa. *Econ. Geol. Bull. Soc. Econ. Geol.* **85**, 663.
- Catling D. C. (2014) 6.7 – The Great Oxidation Event Transition. In *Treatise on Geochemistry* (eds. H. D. Holland and K. K. Turekian), second ed. Elsevier, Oxford, pp. 177–195.
- Cloud P. E. (1965) Significance of the Gunflint (Precambrian) Microflora photosynthetic oxygen may have had important local effects before becoming a major atmospheric gas. *Science* **148**, 27–35.
- Crowe S. A., Døssing L. N., Beukes N. J., Bau M., Kruger S. J., Frei R. and Canfield D. E. (2013) Atmospheric oxygenation three billion years ago. *Nature* **501**, 535–538.
- Dahl T. W., Anbar A. D., Gordon G. W., Rosing M. T., Frei R. and Canfield D. E. (2010) The behavior of molybdenum and its isotopes across the chemocline and in the sediments of sulfidic Lake Cadagno, Switzerland. *Geochim. Cosmochim. Acta* **74**, 144–163.
- Dahl T. W., Chappaz A., Fitts J. P. and Lyons T. W. (2013) Molybdenum reduction in a sulfidic lake: evidence from X-ray absorption fine-structure spectroscopy and implications for the Mo paleoproxy. *Geochim. Cosmochim. Acta* **103**, 213–231.
- Dellwig O., Beck M., Lemke A., Lunau M., Kolditz K., Schnetger B. and Brumsack H.-J. (2007) Non-conservative behaviour of molybdenum in coastal waters: coupling geochemical, biological, and sedimentological processes. *Geochim. Cosmochim. Acta* **71**, 2745–2761.
- Duan Y., Anbar A. D., Arnold G. L., Lyons T. W., Gordon G. W. and Kendall B. (2010) Molybdenum isotope evidence for mild environmental oxygenation before the Great Oxidation Event. *Geochim. Cosmochim. Acta* **74**, 6655–6668.
- Eigenbrode J. L. and Freeman K. H. (2006) Late Archean rise of aerobic microbial ecosystems. *Proc. Natl. Acad. Sci.* **103**, 15759–15764.
- Ellwood B. B., Chrzanowski T. H., Hrouda F., Long G. J. and Buhl M. L. (1988) Siderite formation in anoxic deep-sea sediments: a synergetic bacteria controlled process with important implications in paleomagnetism. *Geology* **16**, 980–982.
- Erickson B. E. and Helz G. R. (2000) Molybdenum (VI) speciation in sulfidic waters: Stability and lability of thiomolybdates. *Geochim. Cosmochim. Acta* **64**, 1149–1158.
- Farquhar J., Bao H. and Thiemens M. (2000) Atmospheric influence of Earth's earliest sulfur cycle. *Science* **289**, 756–758.
- Fischer W., Schroeder S., Lacassie J., Beukes N., Goldberg T., Strauss H., Horstmann U., Schrag D. and Knoll A. (2009) Isotopic constraints on the Late Archean carbon cycle from the transvaal supergroup along the western margin of the Kaapvaal Craton, South Africa. *Precamb. Res.* **169**, 15–27.
- Flament N., Coltice N. and Rey P. F. (2008) A case for late-Archaean continental emergence from thermal evolution models and hypsometry. *Earth Planet. Sci. Lett.* **275**, 326–336.
- Frei R., Gaucher C., Poulton S. W. and Canfield D. E. (2009) Fluctuations in Precambrian atmospheric oxygenation recorded by chromium isotopes. *Nature* **461**, 250–253.
- Goldberg T., Archer C., Vance D. and Poulton S. W. (2009) Mo isotope fractionation during adsorption to Fe (oxyhydr) oxides. *Geochim. Cosmochim. Acta* **73**, 6502–6516.
- Goldberg T., Gordon G., Izon G., Archer C., Pearce C. R., McManus J., Anbar A. D. and Rehkämper M. (2013) Resolution of inter-laboratory discrepancies in Mo isotope data: an intercalibration. *J. Anal. At. Spectrom.* **28**, 724–735.
- Greber N. D., Pettke T. and Nägler T. F. (2014) Magmatic-hydrothermal molybdenum isotope fractionation and its relevance to the igneous crustal signature. *Lithos* **190**, 104–110.
- Hannah J. L., Bekker A., Stein H. J., Markey R. J. and Holland H. D. (2004) Primitive Os and 2316 Ma age for marine shale: implications for Paleoproterozoic glacial events and the rise of atmospheric oxygen. *Earth Planet. Sci. Lett.* **225**, 43–52.
- Helz G., Miller C., Charnock J., Mosselmans J., Pattrick R., Garner C. and Vaughan D. (1996) Mechanism of molybdenum removal from the sea and its concentration in black shales: EXAFS evidence. *Geochim. Cosmochim. Acta* **60**, 3631–3642.
- Helz G. R., Bura-Nakić E., Mikac N. and Ciglenečki I. (2011) New model for molybdenum behavior in euxinic waters. *Chem. Geol.* **284**, 323–332.
- Holland H. D. (2006) The oxygenation of the atmosphere and oceans. *Philos. Trans. Royal Soc. B: Biol. Sci.* **361**, 903–915.
- Jiang G., Kaufman A. J., Christie-Blick N., Zhang S. and Wu H. (2007) Carbon isotope variability across the Ediacaran Yangtze platform in South China: implications for a large surface-to-deep ocean  $\delta^{13}\text{C}$  gradient. *Earth Planet. Sci. Lett.* **261**, 303–320.
- Johnson C. M., Beard B. L., Klein C., Beukes N. J. and Roden E. E. (2008) Iron isotopes constrain biologic and abiologic processes in banded iron formation genesis. *Geochim. Cosmochim. Acta* **72**, 151–169.
- Johnson C. M., Ludois J. M., Beard B. L., Beukes N. J. and Heimann A. (2013) Iron formation carbonates: Paleooceanographic proxy or recorder of microbial diagenesis? *Geology* **41**, 1147–1150.
- Kashiwabara T., Takahashi Y., Tanimizu M. and Usui A. (2011) Molecular-scale mechanisms of distribution and isotopic



- fractionation of molybdenum between seawater and ferromanganese oxides. *Geochim. Cosmochim. Acta* **75**, 5762–5784.
- Kaufman A. J., Hayes J., Knoll A. H. and Germs G. J. (1991) Isotopic compositions of carbonates and organic carbon from upper Proterozoic successions in Namibia: stratigraphic variation and the effects of diagenesis and metamorphism. *Precamb. Res.* **49**, 301–327.
- Kaufman A. J., Johnston D. T., Farquhar J., Masterson A. L., Lyons T. W., Bates S., Anbar A. D., Arnold G. L., Garvin J. and Buick R. (2007) Late Archean biospheric oxygenation and atmospheric evolution. *Science* **317**, 1900–1903.
- Kendall B., Creaser R. A., Gordon G. W. and Anbar A. D. (2009) Re–Os and Mo isotope systematics of black shales from the Middle Proterozoic Velkerri and Wollgorang formations, McArthur Basin, northern Australia. *Geochim. Cosmochim. Acta* **73**, 2534–2558.
- Kendall B., Reinhard C. T., Lyons T. W., Kaufman A. J., Poulton S. W. and Anbar A. D. (2010) Pervasive oxygenation along Late Archaean ocean margins. *Nat. Geosci.* **3**, 647–652.
- Klein C. and Gole M. J. (1981) Mineralogy and petrology of parts of the Marra Mamba Iron Formation, Hamersley Basin, Western Australia. *Am. Mineral.* **66**, 507–525.
- Knauth L. P. and Kennedy M. J. (2009) The late Precambrian greening of the Earth. *Nature* **460**, 728–732.
- Köhler I., Konhauser K. O., Papineau D., Bekker A. and Kappler A. (2013) Biological carbon precursor to diagenetic siderite with spherical structures in iron formations. *Nat. Commun.* **4**, 1741.
- Konhauser K. O., Amskold L., Lalonde S. V., Posth N. R., Kappler A. and Anbar A. (2007) Decoupling photochemical Fe (II) oxidation from shallow-water BIF deposition. *Earth Planet. Sci. Lett.* **258**, 87–100.
- Kowalski N., Dellwig O., Beck M., Gräwe U., Neubert N., Nägler T. F., Badewien T. H., Brumsack H.-J., van Beusekom J. E. and Böttcher M. E. (2013) Pelagic molybdenum concentration anomalies and the impact of sediment resuspension on the molybdenum budget in two tidal systems of the North Sea. *Geochim. Cosmochim. Acta* **119**, 198–211.
- Krapež B., Barley M. E. and Pickard A. L. (2003) Hydrothermal and resedimented origins of the precursor sediments to banded iron formation: sedimentological evidence from the Early Palaeoproterozoic Brockman Supersequence of Western Australia. *Sedimentology* **50**, 979–1011.
- Kurzweil F., Claire M., Thomazo C., Peters M., Hannington M. and Strauss H. (2013) Atmospheric sulfur rearrangement 2.7 billion years ago: evidence for oxygenic photosynthesis. *Earth Planet. Sci. Lett.* **366**, 17–26.
- Liermann L. J., Guynn R. L., Anbar A. and Brantley S. L. (2005) Production of a molybdophore during metal-targeted dissolution of silicates by soil bacteria. *Chem. Geol.* **220**, 285–302.
- Lyons T. W., Werne J. P., Hollander D. J. and Murray R. (2003) Contrasting sulfur geochemistry and Fe/Al and Mo/Al ratios across the last oxic-to-anoxic transition in the Cariaco Basin, Venezuela. *Chem. Geol.* **195**, 131–157.
- McConchie D. (1984) A depositional environment for the Hamersley Group: paleogeography and geochemistry. In *Archean & Proterozoic Basins of the Pilbara, Western Australia: Evolution & Mineralization Potential* (eds. J. Muhling, D. Groves and T. Blake). Geology Department University Extinction, University of Western Australia, pp. 144–195.
- McManus J., Berelson W. M., Severmann S., Poulson R. L., Hammond D. E., Klinkhammer G. P. and Holm C. (2006) Molybdenum and uranium geochemistry in continental margin sediments: paleoproxy potential. *Geochim. Cosmochim. Acta* **70**, 4643–4662.
- Miller C. A., Peucker-Ehrenbrink B., Walker B. D. and Marcantonio F. (2011) Re-assessing the surface cycling of molybdenum and rhenium. *Geochim. Cosmochim. Acta* **75**, 7146–7179.
- Morford J. L. and Emerson S. (1999) The geochemistry of redox sensitive trace metals in sediments. *Geochim. Cosmochim. Acta* **63**, 1735–1750.
- Morris R. (1993) Genetic modelling for banded iron-formation of the Hamersley Group, Pilbara Craton, Western Australia. *Precamb. Res.* **60**, 243–286.
- Morris R. and Horwitz R. (1983) The origin of the iron-formation-rich Hamersley Group of Western Australia—deposition on a platform. *Precamb. Res.* **21**, 273–297.
- Nägler T., Mills M. and Siebert C. (2004) Biological fractionation of Mo isotopes during N<sub>2</sub> fixation by *Trichodesmium* sp. IMS 101. *Geochim. Cosmochim. Acta* **68**, A364.
- Nägler T., Neubert N., Böttcher M., Dellwig O. and Schnetger B. (2011) Molybdenum isotope fractionation in pelagic euxinia: evidence from the modern Black and Baltic Seas. *Chem. Geol.* **289**, 1–11.
- Nägler T. F., Anbar A. D., Archer C., Goldberg T., Gordon G. W., Greber N. D., Siebert C., Sohrin Y. and Vance D. (2014) Proposal for an international molybdenum isotope measurement standard and data representation. *Geostand. Geoanal. Res.* **38**, 149–151.
- Neubert N., Nägler T. F. and Böttcher M. E. (2008) Sulfidity controls molybdenum isotope fractionation into euxinic sediments: evidence from the modern Black Sea. *Geology* **36**, 775–778.
- Ohmoto H., Watanabe Y. and Kumazawa K. (2004) Evidence from massive siderite beds for a CO<sub>2</sub>-rich atmosphere before ~1.8 billion years ago. *Nature* **429**, 395–399.
- Partridge M. A., Golding S. D., Baublys K. A. and Young E. (2008) Pyrite paragenesis and multiple sulfur isotope distribution in late Archean and early Paleoproterozoic Hamersley Basin sediments. *Earth Planet. Sci. Lett.* **272**, 41–49.
- Pavlov A. and Kasting J. (2002) Mass-independent fractionation of sulfur isotopes in Archean sediments: strong evidence for an anoxic Archean atmosphere. *Astrobiology* **2**, 27–41.
- Planavsky N. J., Asael D., Hofmann A., Reinhard C. T., Lalonde S. V., Knudsen A., Wang X., Ossa F. O., Pecoits E. and Smith A. J. (2014) Evidence for oxygenic photosynthesis half a billion years before the Great Oxidation Event. *Nat. Geosci.* **7**, 283–286.
- Poulson Brucker R. L., McManus J., Severmann S. and Berelson W. M. (2009) Molybdenum behavior during early diagenesis: insights from Mo isotopes. *Geochem. Geophys. Geosyst.* **10**.
- Poulson R. L., Siebert C., McManus J. and Berelson W. M. (2006) Authigenic molybdenum isotope signatures in marine sediments. *Geology* **34**, 617–620.
- Poulton S. W., Krom M. D. and Raiswell R. (2004) A revised scheme for the reactivity of iron (oxyhydr) oxide minerals towards dissolved sulfide. *Geochim. Cosmochim. Acta* **68**, 3703–3715.
- Raiswell R. and Canfield D. E. (1998) Sources of iron for pyrite formation in marine sediments. *Am. J. Sci.* **298**, 219–245.
- Reinhard C. T., Planavsky N. J. and Lyons T. W. (2013) Long-term sedimentary recycling of rare sulphur isotope anomalies. *Nature* **497**, 100–103.
- Reinhard C. T., Raiswell R., Scott C., Anbar A. D. and Lyons T. W. (2009) A late Archean sulfidic sea stimulated by early oxidative weathering of the continents. *Science* **326**, 713–716.
- Reitz A., Wille M., Nägler T. F. and de Lange G. J. (2007) Atypical Mo isotope signatures in eastern Mediterranean sediments. *Chem. Geol.* **245**, 1–8.

- Rey P. F. and Coltice N. (2008) Neoproterozoic lithospheric strengthening and the coupling of Earth's geochemical reservoirs. *Geology* **36**, 635–638.
- Rudge J. F., Reynolds B. C. and Bourdon B. (2009) The double spike toolbox. *Chem. Geol.* **265**, 420–431.
- Scott C., Lyons T., Bekker A., Shen Y., Poulton S., Chu X. and Anbar A. (2008) Tracing the stepwise oxygenation of the Proterozoic ocean. *Nature* **452**, 456–459.
- Scott C. and Lyons T. W. (2012) Contrasting molybdenum cycling and isotopic properties in euxinic versus non-euxinic sediments and sedimentary rocks: refining the paleoproxies. *Chem. Geol.* **324**, 19–27.
- Scott C. T., Bekker A., Reinhard C. T., Schnetger B., Krapež B., Rumble D. and Lyons T. W. (2011) Late Archean euxinic conditions before the rise of atmospheric oxygen. *Geology* **39**, 119–122.
- Siebert C., Kramers J., Meisel T., Morel P. and Nögler T. F. (2005) PGE, Re–Os, and Mo isotope systematics in Archean and early Proterozoic sedimentary systems as proxies for redox conditions of the early Earth. *Geochim. Cosmochim. Acta* **69**, 1787–1801.
- Siebert C., McManus J., Bice A., Poulson R. and Berelson W. M. (2006) Molybdenum isotope signatures in continental margin marine sediments. *Earth Planet. Sci. Lett.* **241**, 723–733.
- Siebert C., Nögler T. F., von Blanckenburg F. and Kramers J. D. (2003) Molybdenum isotope records as a potential new proxy for paleoceanography. *Earth Planet. Sci. Lett.* **211**, 159–171.
- Siever R. (1992) The silica cycle in the Precambrian. *Geochim. Cosmochim. Acta* **56**, 3265–3272.
- Simonson B. M., Schubel K. A. and Hassler S. W. (1993) Carbonate sedimentology of the early Precambrian Hamersley Group of Western Australia. *Precamb. Res.* **60**, 287–335.
- Simonson B. M., Sumner D. Y., Beukes N. J., Johnson S. and Gutzmer J. (2009) Correlating multiple Neoproterozoic–Paleoproterozoic impact spherule layers between South Africa and Western Australia. *Precamb. Res.* **169**, 100–111.
- Takano N. (2005) Atlas of Eh–pH diagrams. *Geological survey of Japan open file report*, 102.
- Taylor S. R. and McLennan S. M. (1985). *The continental crust: its composition and evolution*.
- Trendall A., Compston W., Nelson D., De Laeter J. and Bennett V. (2004) SHRIMP zircon ages constraining the depositional chronology of the Hamersley Group, Western Australia\*. *Aust. J. Earth Sci.* **51**, 621–644.
- Trendall A. F., Nelson D. R., De Laeter J. R. and Hassler S. W. (1998) Precise zircon U–Pb ages from the Marra Mamba Iron Formation and Wittenoom Formation, Hamersley Group, Western Australia. *Aust. J. Earth Sci.* **45**, 137–142.
- Tribouillard N., Riboulleau A., Lyons T. and Baudin F. (2004) Enhanced trapping of molybdenum by sulfurized marine organic matter of marine origin in Mesozoic limestones and shales. *Chem. Geol.* **213**, 385–401.
- Tuit C., Waterbury J. and Ravizza G. (2004) Diel variation of molybdenum and iron in marine diazotrophic cyanobacteria. *Limnol. Oceanogr.* **49**, 978–990.
- Voegelin A. R., Nögler T. F., Beukes N. J. and Lacassie J. P. (2010) Molybdenum isotopes in late Archean carbonate rocks: implications for early Earth oxygenation. *Precamb. Res.* **182**, 70–82.
- Voegelin A. R., Pettke T., Greber N. D., von Niederhäusern B. and Nögler T. F. (2014) Magma differentiation fractionates Mo isotope ratios: Evidence from the Kos Plateau Tuff (Aegean Arc). *Lithos* **190**, 440–448.
- Wasylenzi L. E., Rolfe B. A., Weeks C. L., Spiro T. G. and Anbar A. D. (2008) Experimental investigation of the effects of temperature and ionic strength on Mo isotope fractionation during adsorption to manganese oxides. *Geochim. Cosmochim. Acta* **72**, 5997–6005.
- Wichard T., Mishra B., Myneni S. C. B., Bellenger J.-P. and Kraepiel A. M. L. (2009) Storage and bioavailability of molybdenum in soils increased by organic matter complexation. *Nat. Geosci.* **2**, 625–629.
- Widdel F., Schnell S., Heising S., Ehrenreich A., Assmus B. and Schink B. (1993) Ferrous iron oxidation by anoxygenic phototrophic bacteria. *Nature* **362**, 834–836.
- Wille M., Kramers J., Nögler T. F., Beukes N., Schröder S., Meisel T., Lacassie J. and Voegelin A. (2007) Evidence for a gradual rise of oxygen between 2.6 and 2.5 Ga from Mo isotopes and Re–PGE signatures in shales. *Geochim. Cosmochim. Acta* **71**, 2417–2435.
- Wille M., Nögler T. F., Lehmann B., Schröder S. and Kramers J. D. (2008) Hydrogen sulphide release to surface waters at the Precambrian/Cambrian boundary. *Nature* **453**, 767–769.
- Wille M., Nebel O., Van Kranendonk M. J., Schoenberg R., Kleinhanns I. C. and Ellwood M. J. (2013) Mo–Cr isotope evidence for a reducing Archean atmosphere in 3.46–2.76 Ga black shales from the Pilbara Western Australia. *Chem. Geol.* **340**, 68–76.
- Winter B. L. and Knauth L. P. (1992) Stable isotope geochemistry of cherts and carbonates from the 2.0 Ga Gunflint Iron Formation: implications for the depositional setting, and the effects of diagenesis and metamorphism. *Precamb. Res.* **59**, 283–313.
- Woodhead J. D., Hergt J. M. and Simonson B. M. (1998) Isotopic dating of an Archean bolide impact horizon, Hamersley basin, Western Australia. *Geology* **26**, 47–50.
- Zerkle A., Scheiderich K., Maresca J., Liermann L. and Brantley S. (2011) Molybdenum isotope fractionation by cyanobacterial assimilation during nitrate utilization and N<sub>2</sub> fixation. *Geobiology* **9**, 94–106.

Associate editor: Timothy Lyons